J. Fluid Mech. (2023), *vol*. 963, A25, doi:10.1017/jfm.2023.333

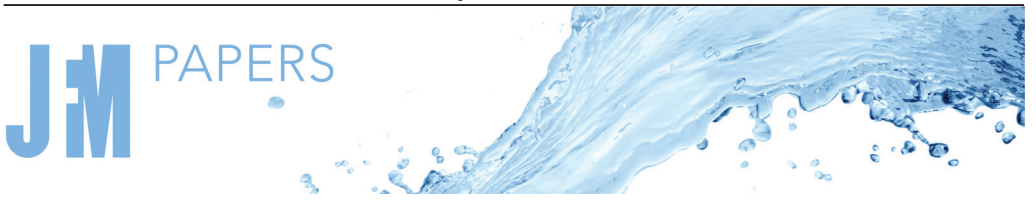

Hydrodynamic instabilities of a dual-mode air–SF_6 interface induced by a cylindrically convergent shock

Yu Liang[1,2], Lili Liu[1,2], Xisheng Luo[1,†] and Chih-Yung Wen[3,†]

[1]Advanced Propulsion Laboratory, Department of Modern Mechanics, University of Science and Technology of China, Hefei 230026, PR China

[2]NYUAD Research Institute, New York University Abu Dhabi, Abu Dhabi 129188, UAE

[3]Department of Aeronautical and Aviation Engineering, The Hong Kong Polytechnic University, Kowloon, Hong Kong

(Received 5 December 2022; revised 17 April 2023; accepted 18 April 2023)

Shock-tube experiments are performed on the convergent Richtmyer–Meshkov (RM) instability of a multimode interface. The temporal growth of each Fourier mode perturbation is measured. The hydrodynamic instabilities, including the RM instability and the additional Rayleigh–Taylor (RT) effect, imposed by the convergent shock wave on the dual-mode interface, are investigated. The mode-coupling effect on the convergent RM instability coupled with the RT effect is quantified. It is evident that the amplitude growths of all first-order modes and second-order harmonics and their couplings depend on the variance of the interface radius, and are influenced by the mode-coupling from the very beginning. It is confirmed that the mode-coupling mechanism is closely related to the initial spectrum, including azimuthal wavenumbers, relative phases and initial amplitudes of the constituent modes. Different from the conclusion in previous studies on the convergent single-mode RM instability that the additional RT effect always suppresses the perturbation growth, the mode-coupling might result in the additional RT effect promoting the instability of the constituent Fourier mode. By considering the geometry convergence, the mode-coupling effect and other physical mechanisms, second-order nonlinear solutions are established to predict the RM instability and the additional RT effect in the cylindrical geometry, reasonably quantifying the amplitude growths of each mode, harmonic and coupling. The nonlinear solutions are further validated by simulations considering various initial spectra. Last, the temporal evolutions of the mixed mass and normalized mixed mass of a shocked multimode interface are calculated numerically to quantify the mixing of two fluids in the cylindrical geometry.

Key words: shock waves

† Email addresses for correspondence: xluo@ustc.edu.cn, chihyung.wen@polyu.edu.hk

© The Author(s), 2023. Published by Cambridge University Press

https://doi.org/10.1017/jfm.2023.333 Published online by Cambridge University Press

1. Introduction

The Richtmyer–Meshkov (RM) instability (Richtmyer 1960; Meshkov 1969) occurs when an interface separating two fluids with different densities is accelerated by a shock wave, then bubbles (lighter fluids penetrating heavier ones) and spikes (heavier fluids penetrating lighter ones) arise, and the turbulence might be finally induced (Zhou *et al.* 2019; Livescu 2020). The RM instability was first theoretically investigated by Richtmyer (1960) and then experimentally confirmed by Meshkov (1969) in the planar geometry. The RM instability is generally regarded as the special Rayleigh–Taylor (RT) instability (Rayleigh 1883; Taylor 1950) at an impulsive limitation. As reviewed by Zhou *et al.* (2021), RM instability plays an essential role in various industrial and scientific fields, including inertial confinement fusion (ICF), supernova explosions, ejecta, material strength, chemical reactions, solar prominence and ionospheric flows. The RM instability on a single-mode interface has been extensively studied due to its fundamental significance (Brouillette 2002; Zhou 2017*a*,*b*; Zhai *et al.* 2018*b*; Liang 2022*a*). Nevertheless, the initial perturbations on the surfaces in applications are essentially multimode with wavenumbers spanning many orders of magnitude (Miles 2004). The relationship between the multimode RM instability and the initial spectrum remains unclear. Furthermore, the ICF and other applications care more about the hydrodynamic instabilities in cylindrical and spherical geometries (Tubbs *et al.* 1999; Glendinning *et al.* 2000; Fincke *et al.* 2004; Smalyuk *et al.* 2014; Peterson *et al.* 2015). Due to its significance, research on the multimode RM instability induced by a convergent shock is urgently needed.

Past studies on the planar multimode RM instability have shown that when the local perturbation on a multimode interface originating from the superposition of multiple modes becomes comparable to its wavelength, the mode-coupling between the multiple modes has an important influence on the instability development (Haan 1989). The following theoretical, experimental and numerical works on the planar multimode RM instability are introduced below.

(i) Theoretically, Haan (1991) first proposed a modal model with second-order accuracy to quantify the influence of the mode-coupling between the multiple modes on the RT instability. The modal model and its extended types have achieved a wide range of validation in the issues of RT instability (Remington *et al.* 1995; Ofer *et al.* 1996; Elbaz & Shvarts 2018) and RM instability (Liang *et al.* 2021). Assuming that the mode-coupling is absent before each bubble of a multimode RM unstable interface reaches its asymptotic growth, Alon *et al.* (1994) proposed a statistical potential flow model to predict the eventual average bubble distribution and bubble amplitude growth rate. However, the potential flow model is invalid when the two fluids' densities are similar. Subsequently, Rikanati, Alon & Shvarts (1998) proposed the vortex model to make up the bubble asymptotic growth rate when the density ratio of the two fluids approaches unity. Both the potential flow model (Alon *et al.* 1994, 1995; Oron *et al.* 2001) and the vortex model (Rikanati *et al.* 1998) acquire a self-similar growth of the bubble amplitude independent of the initial spectrum. Later, the perturbation expansion model (Zhang & Sohn 1997) was extended by Vandenboomgaerde, Gauthier & Mügler (2002) to predict the early nonlinear amplitude growths of the constituted modes of a multimode RM unstable interface by retaining the terms with the highest power in time. Recently, the group theory approach (Abarzhi 2008, 2010; Pandian, Stellingwerf & Abarzhi 2017) has been proven to identify the connection between the symmetry properties of the interface morphology and the relative phases of the modes constituting the interface spectrum.

(ii) Experimentally, Sadot *et al.* (1998) performed the first shock tube experiments to investigate the two-bubble competition and found that the bubbles with a larger size expand

https://doi.org/10.1017/jfm.2023.333 Published online by Cambridge University Press

and rise faster, whereas the bubbles with a smaller size shrink and are swept downstream into the spikes of surviving bubbles. Dimonte & Schneider (2000) conducted a series of three-dimensional linear electric motor experiments to investigate the multimode RT and RM instabilities. They found that the density ratio has a limited effect on the self-similar growth factor θ for the bubble. When the density ratio is large, the θ for the spike is larger than the bubble counterpart. Niederhaus & Jacobs (2003) investigated the multimode RM instability of two liquids and found that the development of the multimode perturbation strongly depends on the amplitudes of the initially constituent modes. Balasubramanian, Orlicz & Prestridge (2013) argued that the growth of the multimode perturbation created by a gas curtain shows a weak dependence on the initial spectra. Di Stefano *et al.* (2015*a*,*b*) performed the RM instability experiments of a dual-mode interface under high-Mach-number conditions. The results indicated that new harmonics are generated from the mode-coupling between the two initially constituent modes, and the perturbations of these modes grow and saturate over time. The dual-mode RM instability under weak shock conditions was considered by Luo *et al.* (2020), from which the mode-coupling effect on the RM instability cannot be ignored when the wavenumber of one constituted mode is twice the wavenumber of the other constituted mode. Mohaghar *et al.* (2017) experimentally investigated the mixing of a multimode RM unstable interface using density and velocity statistics and found that the flow shows distinct memory of initial conditions. The long-wavelength perturbation has a strong influence on the interface development. Liang *et al.* (2019) examined the RM instability on four quasi-single-mode interfaces created by the soap film technique in the early nonlinear stage. The effect of initially constituent high-order modes on the multimode RM instability was highlighted to distinguish the multimode RM instability from the single-mode counterpart. Guo *et al.* (2022) further confirmed that the RM instability of a quasi-single-mode interface still has memory on the initial spectrum even though the interface is shocked twice. Mansoor *et al.* (2020) generated a near-sinusoidal interface dominated by one mode with a novel membraneless technique where cross-flowing air is separated from SF_6 by an oscillating splitter plate. Earlier mixing transitions for higher amplitude-to-wavelength ratio cases were noted from the experiments. Liang *et al.* (2021) investigated the RM instability on a multimode air–SF_6 interface initially dominated by three modes. It was revealed that the mode-coupling is closely related to the initial spectrum and plays an essential role in RM flows from the very beginning if the initial amplitudes of the constituent modes are large. Liang, Liu & Luo (2022) examined the differences between the effects of bubble competition and spike competition on the multimode RM instability and concluded that the bubble competition suppresses instability of the small-wavelength perturbation more than the spike competition.

(iii) Numerically, it is commonly realized that the phases of the constituted modes influence the multimode perturbation growth (Vandenboomgaerde *et al.* 2002; Miles *et al.* 2004; Pandian *et al.* 2017). Besides, the self-similar growth factor θ of the late-time RM instability depends on the scale of the initial spectrum. Although the values of θ in many high-fidelity simulations, including the extensive collaborations of the θ-group (Thornber *et al.* 2017), have not been unified, it is widely accepted that the broadband perturbation leads to a larger bubble growth factor than the narrowband counterpart (Thornber *et al.* 2010; Liu & Xiao 2016; Thornber 2016; Groom & Thornber 2020).

The convergent RM instability, involving initial conditions relevant to the ICF, has become increasingly attractive in recent years (Zhou 2017*a*; Zhou *et al.* 2021). Compared with the planar RM instability, the convergent RM instability involves more physical mechanisms. First, the unique geometric convergence inevitably influences the convergent

https://doi.org/10.1017/jfm.2023.333 Published online by Cambridge University Press

RM instability. For example, in a high-gain ICF target, the ratio of the initial outer target radius to the final hot-spot radius is up to ∼30–40. Second, the additional RT effect induced by the acceleration or deceleration of the interface complicates the interface evolution and results in the interface being more unstable or stable. Third, the compressibility of the postshock flow further influences the instability. Other theoretical, experimental and numerical works on the convergent RM instability are introduced below.

(i) Theoretically, based on the small perturbation assumption, Bell (1951) and Plesset (1954) separately derived the linear solutions for the convergent RM instability in the cylindrical and spherical geometries. It was found that the interface amplitude growth rate varies with the radius of the shocked interface, which is later called the Bell–Plesset effect. Amendt *et al.* (2003) further considered the case where the densities of the two fluids change uniformly with time. Later, Epstein (2004) deduced a compressible linear solution for the convergent RM instability accounting for the fluid compression. Mikaelian (1990, 2005) examined the convergent RM instability of multiple interfaces in cylindrical and spherical geometries and proposed a numerical method to solve the eigenvalue problems of the convergent RM instability on the arbitrary number of stratified fluids. In the same order of the geometry convergence, Mikaelian (2005) separately listed the linear solutions for the planar, cylindrically convergent and spherically convergent RM instability using the impulsive acceleration assumption (Richtmyer 1960) as

$$a_n = a_n^0(1 + kA\Delta vt), \tag{1.1}$$

$$a_n = a_n^0\left[1 + (nA - 1)\left(1 - \frac{R_i^0}{R_i}\right)\right], \tag{1.2}$$

$$a_n = a_n^0\left\{1 + \left[\frac{n(n+1)A}{2n + 1 - A} - 1\right]\left[1 - \left(\frac{R_i^0}{R_i}\right)^2\right]\right\}, \tag{1.3}$$

where a_n and a_n^0 are the time-varying amplitude and the initial amplitude of the single-mode perturbation with the azimuthal wavenumber n ($\equiv kR_i$), respectively; k is the wavenumber of the single-mode perturbation; R_i and R_i^0 are the time-varying radius and the initial radius of the interface, respectively; Δv is the velocity jump of the interface induced by the shock; and A (defined as $(\rho^{ex} - \rho^{in})/(\rho^{ex} + \rho^{in})$, with ρ^{ex} and ρ^{in} being the density of the external fluid located at a radius r of $r > R_i$ and the density of the inner fluid located at $R_i > r > 0$, respectively, as sketched in figure 1*d*) is the Atwood number. Assuming that the interface moves uniformly, i.e. $R_i = R_i^0 + \Delta vt$, (1.2) and (1.3) separately for the cylindrically and spherically convergent RM instability reduce to (1.1) for the planar RM instability at a large R_i. Recently, based on the perturbation expansion method, Liu, He & Yu (2012) derived a fourth-order weakly nonlinear solution for the RM instability of a single-mode interface at a fixed radial position in the cylindrical geometry, highlighting the cylindrical geometry effect on bubbles and spikes under different A conditions. Subsequently, Liu *et al.* (2014) extended the validity range of the weakly nonlinear solution (Liu *et al.* 2012) to the late nonlinear stage based on Padé approximation, and which agrees well with the numerical results of Matsuoka & Nishihara (2006). Wang *et al.* (2015) proposed a weakly nonlinear solution for the cylindrically convergent RM instability of a uniformly imploding or exploding single-mode interface. The perturbation growths of the first three-order harmonics and the high-order feedback to the fundamental mode were quantified.

https://doi.org/10.1017/jfm.2023.333 Published online by Cambridge University Press

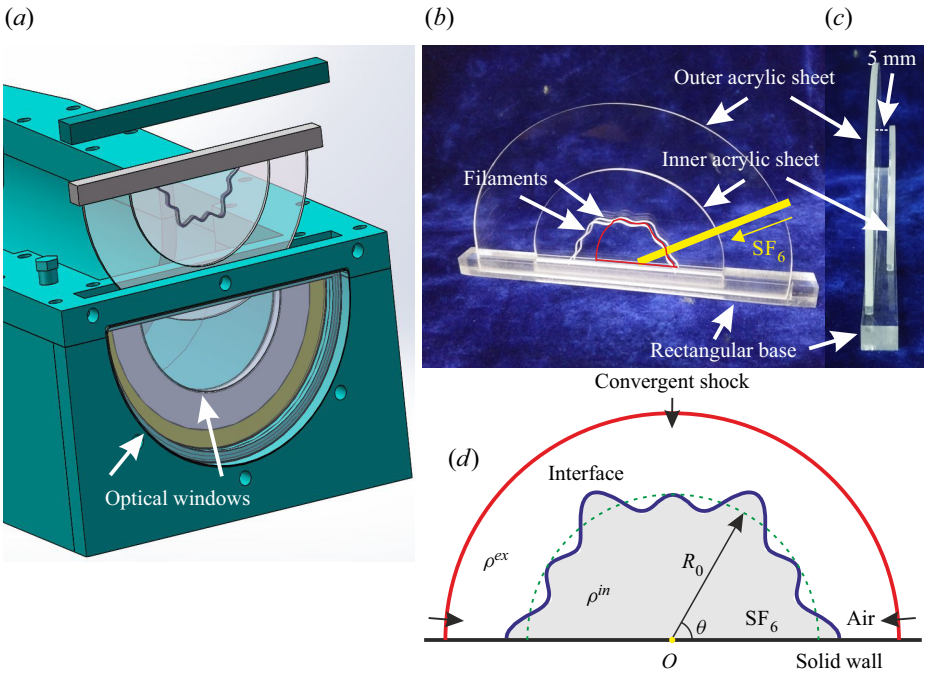

Figure 1. (*a*) Sketch of the test section of the semiannular shock tube, (*b*) the front view and (*c*) the side view of the interface formation device and (*d*) the experimental configuration for a cylindrically convergent shock impacting a dual-mode air–SF_6 interface: R_i^0 denotes the radius of the balanced position of the initial dual-mode interface; O denotes the geometric centre; and ρ^{ex} and ρ^{in} denote the densities of the fluids located at a radius r of $r > R_i$ and $R_i > r > 0$, respectively.

(ii) Experimentally, Hosseini & Takayama (2005) used double-exposure holographic interference technology to capture the interaction of a cylindrically convergent shock and a gas cylinder with various species in an annular vertical diaphragmless shock tube. The mixed width growth rate of the reshocked interface in the cylindrical geometry was found to be larger than that in the planar geometry. Recently, Si *et al.* (2015) and Lei *et al.* (2017) improved the interface formation and flow visualization methods in the same kind shock tube. The interactions of a cylindrically convergent shock and various polygonal and sinusoidal air–SF_6 interfaces were experimentally investigated. Based on the gas lens method (Dimotakis & Samtaney 2006) to convert a planar shock to a convergent shock, the cylindrically convergent RM instability on the single-mode SF_6–air interface (Biamino *et al.* 2015; Vandenboomgaerde *et al.* 2018*a*) and air–SF_6 interface (Biamino *et al.* 2017; Vandenboomgaerde *et al.* 2018*b*) were separately investigated. The influence of the supports utilized to form the initial nitrocellulose interface on the RM flow was investigated (Vandenboomgaerde *et al.* 2018*a*). Recently, Brasseur *et al.* (2021) extended the gas lens method to generate a spherically convergent shock and showed the potential to perform spherically convergent RM instability experiments. Zhai *et al.* (2010, 2012) designed a curved solid wall with a specific shape to directly convert a planar shock to a cylindrically convergent shock according to the shock dynamics in a horizontal shock tube. Subsequently, the interactions of a cylindrically convergent shock and various interfaces, including gas bubbles, gas cylinders, inclined interfaces and sinusoidal interfaces, were experimentally investigated in this shock tube (Si, Zhai & Luo 2014*a*; Si *et al.* 2014*b*; Zhai *et al.* 2017; Liang, Zhai & Luo 2018; Luo *et al.* 2014, 2018, 2019). In these works, Luo *et al.*

https://doi.org/10.1017/jfm.2023.333 Published online by Cambridge University Press

(2018) studied the convergent RM instability on a three-dimensional air–SF_6 single-mode interface with a minimum-surface feature. They observed the interface deceleration due to the high pressure near the geometric centre. It was proved that the interface deceleration leads to the additional RT effect superposed on the evolving interface, resulting in a rapid decrease in the interface amplitude, and even causing the phase reversal of the interface before the reshock. To eliminate the interface deceleration and the additional RT effect, Luo *et al.* (2019) transferred the cylindrically convergent shock to a planar one when the transmitted shock is near the geometric centre, avoiding the high pressure near the geometric centre. Recently, the shock dynamics method has been extended to generate a spherically convergent shock (Kjellander, Tillmark & Apazidis 2012; Liverts & Apazidis 2016; Sembian & Liverts 2020) and a cylindrically divergent shock (Li *et al.* 2020*b*). Moreover, Luo *et al.* (2015) designed a semiannular horizontal shock tube to generate a cylindrically convergent shock and showed its great potential in studying the convergent RM instability due to the convenience of forming shape-controllable gaseous interfaces. Subsequently, Ding *et al.* (2017*a*) examined the time-varying interface displacement of a shocked unperturbed air–SF_6 interface and the amplitude growths of a single-mode air–SF_6 interface with various amplitude-to-wavelength ratios in this shock tube. Recently, a series of experimental studies on the hydrodynamic instabilities of a gas layer driven by a cylindrically convergent shock has been conducted in this shock tube (Ding *et al.* 2019; Sun *et al.* 2020; Ding, Deng & Luo 2021; Li *et al.* 2020*a*, 2022). It was revealed that the mode-coupling between the two interfaces of the gas layer and the reverberating waves inside the gas layer have non-negligible influences on the gas layer evolution.

(iii) Numerically, Zhang & Graham (1997) discovered the scaling laws for the RM unstable interface driven by a strong cylindrically convergent shock. Later, Zhang & Graham (1998) performed a series of simulations on the RM instability of a single-mode interface driven by a cylindrically convergent or divergent shock and observed the complex instability development after the reshock. Matsuoka & Nishihara (2006) numerically investigated the interface evolution using the vortex dynamics method in the cylindrical geometry. They analysed the curvatures of bubbles and spikes as well as the vorticity strength and circulation on the evolving interface. Lombardini & Pullin (2009*b*) studied the linear evolution of the convergent RM instability and deduced a unified expression for the asymptotic growth rate of the planar, cylindrical and spherical RM instability, highlighting the influence of the geometric convergence on the perturbation growth rate. Lombardini, Pullin & Meiron (2014) performed a large-eddy simulation on the spherically convergent RM instability. It was found that the reshock mixing on an air–SF_6 interface is enhanced by the reverberating shocks between the interface and the geometric centre, which is different from the planar RM instability that is enhanced by the reverberating rarefaction waves between the interface and the reflection wall. Wu, Liu & Xiao (2021) compared their simulations with the experiments of Lei *et al.* (2017) using the direct numerical simulation method. They concluded that both qualitative and quantitative consistencies between simulations and experiments could be achieved before the reshock provided that the premixed width of the interface is taken into account. Li *et al.* (2021) investigated the convergent RM instability in cylindrical and spherical geometries using the implicit large-eddy simulation method, highlighting the differences in the statistical characteristics of turbulent mixing between the cylindrically and spherically convergent RM instability. Yan *et al.* (2022) investigated the cylindrically convergent RM instability with and without chemical reactions using the direct numerical simulation method to explore the influence of chemical reactions on the statistical characteristics of transition and turbulent mixing.

https://doi.org/10.1017/jfm.2023.333 Published online by Cambridge University Press

From the reviews of the multimode RM instability and the convergent RM instability, it is evident that the RM instability is related to the initial spectrum and the geometric domain. However, the quantitative relation between initial conditions and the multimode RM instability driven by a convergent shock is still unclear. On the one hand, elaborate convergent shock tube experiments on the multimode RM instability with controllable initial conditions are very limited. On the other hand, analytical models for predicting the multimode RM instability in cylindrical and spherical geometries are rare. In this work, experiments are performed for the first time on the convergent RM instability of a multimode interface in a shock-tube facility, and the temporal growth of each Fourier mode perturbation is measured. The mode-coupling effect on the convergent RM instability coupled with the RT effect is quantified for the first time. The different contributions of the mode-coupling to the hydrodynamic instabilities of the multimode interface and single-mode interface are highlighted. Second-order nonlinear solutions are developed to predict the multimode RM instability and the additional RT effect in the cylindrical geometry. Numerical simulations are also performed to provide quantitative data considering more initial conditions. The temporal evolutions of the mixed mass and normalized mixed mass of a shocked multimode interface are calculated for the first time to quantify the mixing of two fluids in the cylindrical geometry.

2. Experimental and numerical methods

2.1. *Experimental set-up*

The experiment is carried out in a semiannular convergent shock tube originally designed by Luo *et al.* (2015), which has exhibited good feasibility and reliability in producing a cylindrically convergent shock (Liang *et al.* 2017; Ding *et al.* 2017*a*, 2019, 2021; Sun *et al.* 2020; Li *et al.* 2020*a*, 2022). The main difficulty for performing an experimental study on the multimode RM instability, especially in a convergent shock tube circumstance, lies in creating an idealized initial interface because the RM instability is extremely sensitive to the initial conditions. Benefiting from the open test section, as sketched in figure 1(*a*), a removable interface formation device can be efficiently designed in which a shape-controllable gaseous interface can be generated using the extended soap film technique. The soap film technique can essentially eliminate the additional short-wavelength perturbations, diffusion layer and three-dimensionality (Liu *et al.* 2018; Liang *et al.* 2021). As shown in figures 1(*b*) and 1(*c*), a device consisting of two semicircular transparent acrylic sheets with a spacing of 5.0 mm is fixed on a rectangular base. Two microchannels (with a width of 0.50 mm and a depth of 0.20 mm) with a designed dual-mode shape are precisely engraved on the opposite surfaces of the two acrylic sheets. Two acrylic filaments (with a width of 0.45 mm and a height of 0.40 mm) with the same dual-mode shape are embedded separately in the microchannels to introduce two small bulges on the plate surfaces to restrict the soap film. Subsequently, a soap bubble full of SF_6 is blown within two plates through an injection tube (as marked in yellow in figure 1*b*). The soap bubble expands continuously along the filaments. When the volume of the soap bubble is approximately 2/3 of the constraint space (as marked in red in figure 1*b*), we stop injecting the SF_6 and immediately insert the interface formation device into the test section and equipped tightly with optical windows, as shown in figure 1(*a*). Because the density of SF_6 is much greater than that of air, it is easier for air to permeate into the soap film. Therefore, the soap bubble will keep swelling after removing the injection tube. When the soap bubble just thoroughly contacts the filaments and a sinusoidal boundary

https://doi.org/10.1017/jfm.2023.333 Published online by Cambridge University Press

at the interface is formed, the shock wave is generated immediately and the experiment is performed.

The experimental configuration is sketched in figure 1(*d*), where a cylindrically convergent shock moves inward and later impacts the dual-mode interface. In a polar coordinate system, the initial interface can be parameterized as

$$r = R_i^0 + a_{n_1}^0 \cos(n_1\theta) + a_{n_2}^0 \cos(n_2\theta), \tag{2.1}$$

where R_i^0 equals 26.0 mm; n_1 and n_2 denote the azimuthal mode numbers of the two initially constituent modes and equal 6 and 12, respectively, in the experiment; and the initial amplitudes of mode n_1 ($a_{n_1}^0$) and mode n_2 ($a_{n_2}^0$) equal 1.0 mm.

The ambient pressure and temperature are 101.33 kPa and 293.15 K, respectively. In the experiment, the shock velocity at the time of the impact with the interface cannot be obtained precisely due to the limitation of temporal resolution. However, the Mach number of the incident shock at a radius of 34.0 mm, i.e. before the shock reaches the interface, can be measured to be 1.29 ± 0.01. The increment of the shock Mach number between that instant and when the shock reaches the interface is approximately 0.03, according to the Chester–Chiness–Whitham relations (Chester 1954; Chisnell 1957; Whitham 1958). As a result, the Mach number of the incident converging shock at the interface's impact time is evaluated to be 1.32 ± 0.01.

The ambient gas is air, and the test gas is a mixture of air and SF_6. The mass fraction of SF_6 is deduced as 91.1 % according to the one-dimensional gas dynamics theory (Drake 2018) and the velocities of the incident shock and the shock reflected from the interface after the incident shock impacts the interface. The Atwood number A is -0.57 in this study. When the shock impacts the initial interface, the velocity of the incident shock (v_s) in the air is -457 m s^{-1}, the velocity of the transmitted shock (v_t) in the mixture of air and SF_6 is -236 m s^{-1}, the velocity of the reflected shock in the air (v_f) is 407 m s^{-1} and the velocity jump of the interface (Δv) is -123 m s^{-1}.

The flow field is illuminated by a direct-current-regulated light source (CEL-HXF300, the maximum power output is 249 W) and captured by schlieren photography combined with a high-speed camera (FASTCAM SA5, Photron Limited, with full resolution of 1024×1024). The camera's frame rate is 87 500, corresponding to a time interval of 11.43 μs. The exposure time is 1 μs. The pixel resolution is 0.26 mm pixel^{-1}.

2.2. *Numerical scheme*

Numerical simulations are performed to obtain the detailed flow field required for an in-depth analysis of flow regimes. The process of a cylindrically convergent shock interacting with a gaseous interface examined in this study is described by compressible Euler equations, which coincide with the numerical studies focusing on the early-to-intermediate regimes of RM instability with or without the reshock (Grove *et al.* 1993; Holmes & Grove 1995; Holmes *et al.* 1999; Herrmann, Moin & Abarzhi 2008; Niederhaus *et al.* 2008; Leinov *et al.* 2009; Ding *et al.* 2017*b*, 2018; Zhai *et al.* 2017, 2018*a*; Zhai, Ou & Ding 2019*a*; Zhai *et al.* 2019*b*; Zou *et al.* 2019; Igra & Igra 2020; Zhou *et al.* 2020*b*; Tang *et al.* 2021). An upwind space–time conservation elements/solution elements scheme is utilized with second-order accuracy in both space and time (Shen *et al.* 2015*a*; Shen, Wen & Zhang 2015*b*; Shen & Wen 2016). A volume-fraction-based five-equation model (Abgrall 1996; Shyue 1998) is used to illustrate the different species residing on both sides of the inhomogeneous interface. The contact discontinuity restoring Harten–Lax–van Leer contact Riemann solver (Toro, Spruce & Speares 1994) is used

https://doi.org/10.1017/jfm.2023.333 Published online by Cambridge University Press

to determine the numerical fluxes between the conservation elements. The use of this scheme in capturing shocks and details of complex flow structures for the RM instability issues and shock–droplet interactions have been well validated (Shen *et al.* 2017; Shen & Parsani 2017; Guan *et al.* 2018; Fan *et al.* 2019; Zhai *et al.* 2017, 2019*b*; Zhou *et al.* 2020*b*; Liang *et al.* 2020; Liang 2022*b*; Liang & Luo 2023). A comprehensive review of the numerical scheme and its extensive applications was recently reported by Jiang, Wen & Zhang (2020).

The initial settings of the two-dimensional simulation are presented in figure 2(*a*). Open boundary conditions, which apply a zeroth-order extrapolation of physical quantities to ghost points, are enforced on the left-hand, right-hand and bottom boundaries ($x = -100.0$, $x = 100.0$ and $y = 50.0$ mm), respectively, to eliminate the waves reflected from the left-hand, right-hand and bottom boundaries (Zhai *et al.* 2019*b*; Zhou *et al.* 2020*b*). Reflection conditions are imposed at the top boundary ($y = 0$). The density and specific heat ratio of the ambient gas outside the perturbed gas cylinder are 1.20 kg m^{-3} and 1.40, respectively; and the density and specific heat ratio of the test gas inside the perturbed gas cylinder are 4.46 kg m^{-3} and 1.127, respectively. The initially incident shock wave is set to travel inward with a Mach number of 1.29 and a radius of 34.0 mm, as sketched in figure 2(*a*). The initial postshock flow is supposed to be uniform and calculated according to the Rankine–Hugoniot relation, which coincides with the recent numerical studies on the convergent RM instability (Zhai *et al.* 2019*b*; Zhou *et al.* 2020*b*; Li *et al.* 2021; Tang *et al.* 2021; Wu *et al.* 2021; Yan *et al.* 2022).

2.3. *Code validation*

We measure the mixed width from experimental schlieren images and compare it with numerical simulations. We measure the distances between the geometry centre and four crests of a dual-mode interface, as shown in figure 2(*a*), and calculate the average value as the radius of the crest, i.e. r_S. Similarly, we measure distances between the geometry centre and six troughs of a dual-mode interface and calculate the average value as the radius of the trough, i.e. r_B. The mixed with, w, is defined as $r_S - r_B$.

For the data obtained from numerical simulations, since the mass fraction of SF_6 in the test gas is decided by the experiment as 91.1 %, we choose the nodes with a mass fraction of SF_6 between 1.0 % and 90.0 % as the interfacial contour. Then, the mean radius of these nodes on each azimuthal angle is taken as the average position of the local interface. The mixed width w in simulations is defined as the maximum radial distance between the crest and trough of a dual-mode interface, as sketched in figure 2(*a*).

The time-varying dimensionless mixed width of the dual-mode interface is measured from experiments, as shown with solid symbols in figure 2(*b*). The moment when the incident shock reaches the radius of R_i^0 is defined as $t = 0$. Time is scaled as $\tau = t\Delta v/R_i^0$, and mixed width is scaled as $\omega = w/w_0$, where w_0 denotes the initial mixed width of the dual-mode interface and equals 3.12 mm in the experiment. It can be found that the current numerical results, as shown with lines in figure 2(*b*), quantitatively agree well with the experimental results. Four mesh sizes of 0.20 mm, 0.10 mm, 0.05 mm and 0.025 mm are tested for the grid-convergence validation. The time-varying dimensionless mixed widths of the dual-mode interface converge when the mesh size is reduced to 0.05 mm and 0.025 mm in the numerical simulations. Therefore, an initial mesh size of 0.05 mm is adopted for all simulations to ensure accuracy and minimize the computational cost.

https://doi.org/10.1017/jfm.2023.333 Published online by Cambridge University Press

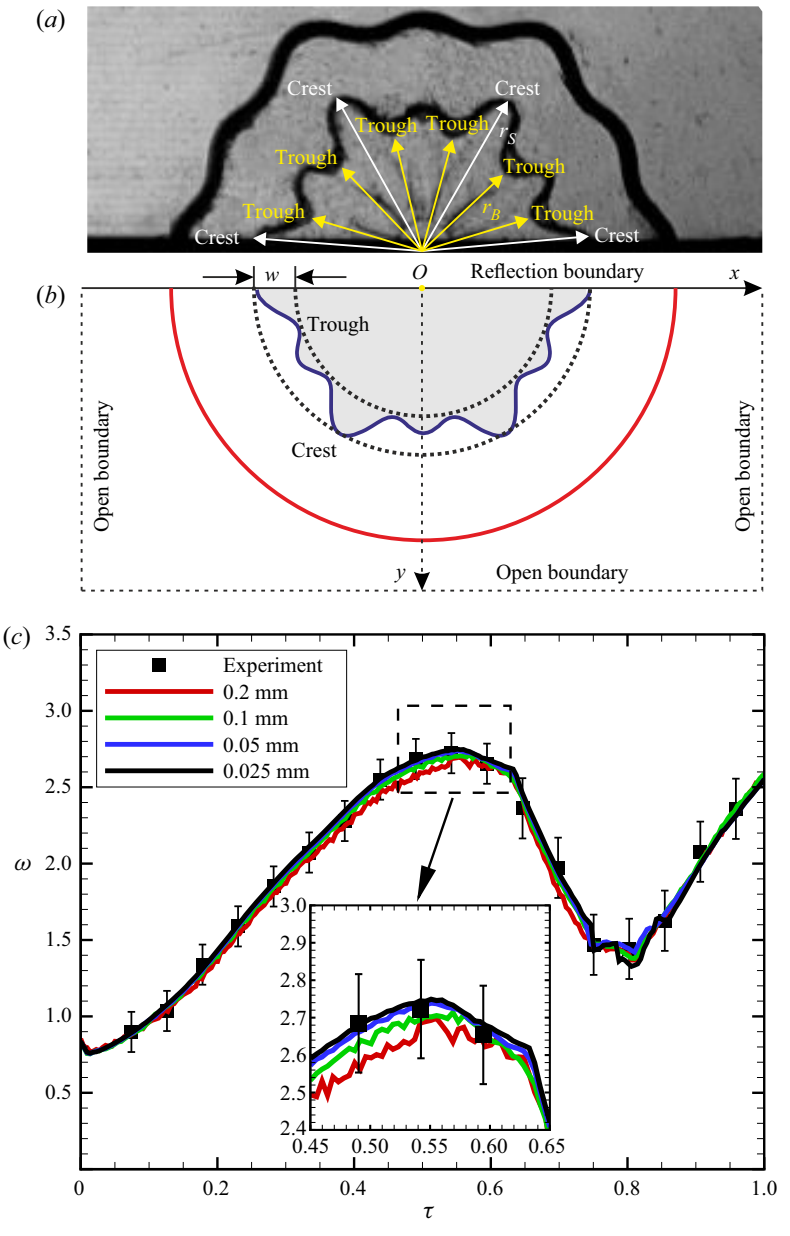

Figure 2. (*a*) Measurements of the radii of the crest (r_S) and the trough (r_B) of a dual-mode interface from experimental schlieren images. (*b*) Schematics of the numerical set-up, with w denoting the mixed width of the dual-mode interface. (*c*) Comparisons of the dimensionless mixed width of the dual-mode interface between the experimental results and numerical results at different mesh sizes. The red semicircle in (*b*) at $r = 34$ mm indicates the initial imploding shock of Mach number 1.29.

3. Qualitative analysis

The initial dual-mode interface (II) in the experiment has a short-wavelength spike (SS) in the middle with two long-wavelength spikes (LS) located on its two sides, as shown in figure 3. Before the shock impacts the interface (-7 μs), the initial interface in the schlieren image seems thick because the interface is covered by two dual-mode

https://doi.org/10.1017/jfm.2023.333 Published online by Cambridge University Press

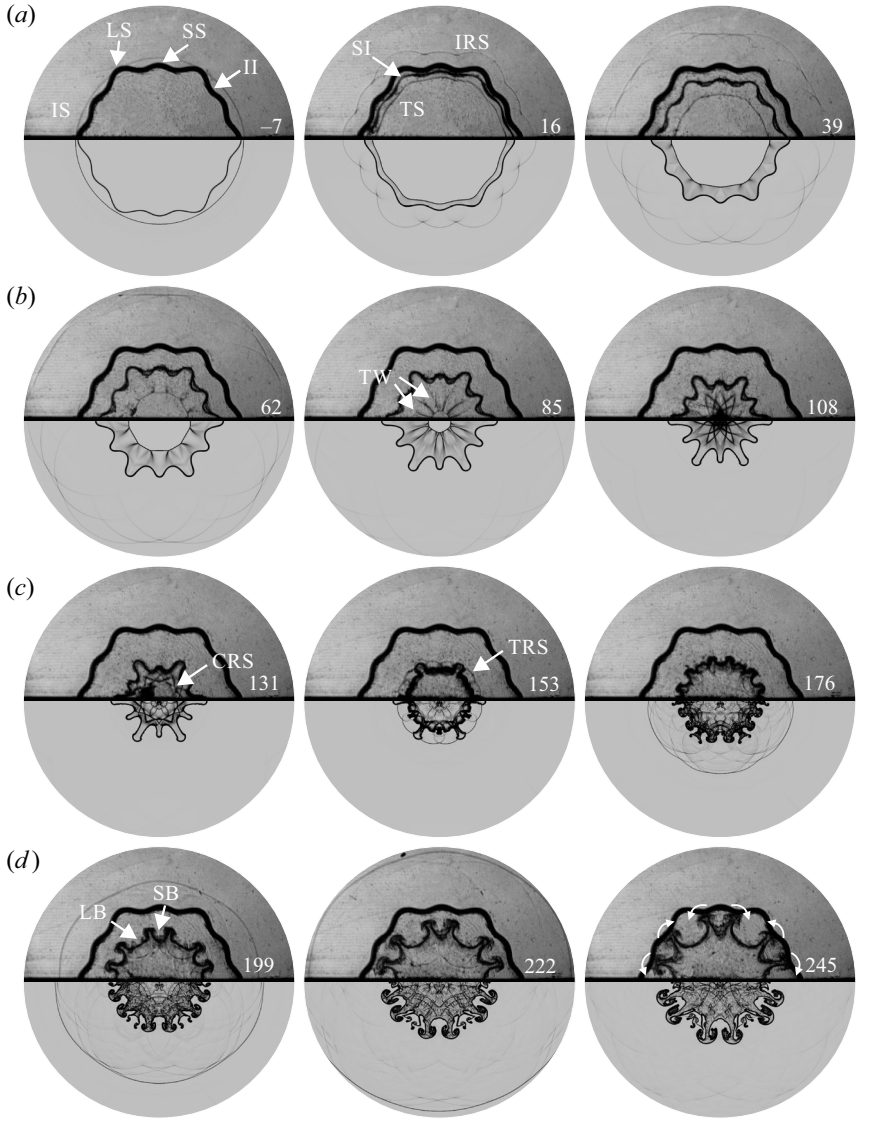

Figure 3. Typical schlieren images obtained from the experiment (top half of each image) and simulation (bottom half), where IS denotes the incident convergent shock, II denotes the initial interface, LS denotes the long-wavelength spike, SS denotes the short-wavelength spike, LB denotes the long-wavelength bubble, SB denotes the short-wavelength bubble, TS denotes the transmitted shock, IRS denotes the shock reflected from the initial interface, SI denotes the shocked interface, TW denotes the transverse waves, CRS denotes the shock reflected from the geometric centre and TRS denotes the transmitted reflection shock. Curved white arrows represent the orientations that spikes skew towards, and numbers in the images indicate time in microseconds. The moment when the incident shock reaches the radius of R_i^0 is defined as $t = 0$.

microchannels (0.5 mm in width) engraved on the transparent acrylic sheets. First, when the incident shock (IS) passes across the interface, the shock bifurcates into an inward-moving transmitted shock (TS) and an outward-moving reflected shock (IRS). Subsequently, the shocked interface (SI) leaves its original location, and a density-gradient interface with a perfect dual-mode shape can be observed (16 μs). As time proceeds, the

https://doi.org/10.1017/jfm.2023.333 Published online by Cambridge University Press

interface undergoes sustained deformation due to the deposition of baroclinic vorticity induced by the incident shock and the geometry convergence (Lombardini & Pullin 2009*b*; Ding *et al.* 2017*a*; Vandenboomgaerde *et al.* 2018*a*). Our previous study (Liang *et al.* 2017) found that the perturbation on the TS reduces gradually as the shock converges, which is similar to the planar case where the disturbances on a planar shock front are known to die out (Bates 2004). However, as the TS converges, the undisturbed shock radius (the distance from the undisturbed cylindrical shock front to the geometry centre) also reduces, and the ratio of perturbation of the TS to the radius of the TS actually increases. As a result, the front of the convergent TS becomes polygonal (Apazidis & Lesser 1996; Apazidis *et al.* 2002; Lei *et al.* 2017), and the transverse waves (TW) behind the transmitted shock are prominent (85 μs).

After the transmitted shock focuses at the geometric centre around 108 μs, a central reflected shock (CRS) forms and moves outwards (131 μs). Later, the CRS impacts the evolving dual-mode interface (153 μs), leading to the phase reversal of the dual-mode interface (Brouillette 2002). The perturbation on the dual-mode interface first decreases to a minimal value (176 μs) and then increases with an opposite phase to the initial interface perturbation (199 μs). The reshocked interface consists of a short-wavelength bubble (SB) in the middle with two long-wavelength bubbles (LB) on its two sides. Last, shocks and rarefaction waves are reflected with decreasing strengths between the interface and the geometric centre. The competition and coalescence of large coherent structures drive the bubble-merging (Sadot *et al.* 1998; Oron *et al.* 2001; Srebro *et al.* 2003) on the reshocked dual-mode interface, resulting in the spikes skewing towards the long-wavelength bubbles (see the white arrows in the 245 μs image).

The magnitude of the density-gradient field in the simulation is calculated as (Quirk & Karni 1996; Sembian, Liverts & Apazidis 2018)

$$|\nabla \rho| = \left[\left(\frac{\partial \rho}{\partial x} \right)^2 + \left(\frac{\partial \rho}{\partial y} \right)^2 \right]^{1/2}. \tag{3.1}$$

The numerical results are shown in the bottom half of the images in figure 3. It can be observed that both waves and interfacial morphologies in simulations qualitatively agree well with the experimental results.

4. Quantitative analysis

4.1. *Experimental and numerical results*

Due to the nonlinearity of the RM instability (Velikovich & Dimonte 1996; Nishihara *et al.* 2010; Guo *et al.* 2014; Wang *et al.* 2015), the two initially constituent modes, i.e. modes n_1 and n_2, generate two harmonics with wavenumbers $2n_1$ and $2n_2$, respectively. Moreover, the mode-coupling between the two initially constituent modes generates two couplings with wavenumbers $n_2 + n_1$ and $n_2 - n_1$ (Haan 1989, 1991; Ofer *et al.* 1992).

The captured interface morphology is distinct such that the interfacial contour in the experiment can be extracted by an image processing program (Luo *et al.* 2020; Liang *et al.* 2021), as indicated by the inset in figure 4. Spectral analysis is then performed on the coordinate of the interfacial contour before the interface is reshocked. Notably, since $n_2 = 2n_1$ and $n_1 = n_2 - n_1$ in the experiment, the harmonic $2n_1$ and coupling $n_2 - n_1$ are superposed on the mode n_2 and mode n_1, respectively. The time-varying amplitudes of modes n_1 and n_2 and the new harmonic $2n_2$ and coupling $n_2 + n_1$ are then acquired, as shown with square symbols for the experiment and circle symbols for the simulation in figure 4. The amplitude of the mode, harmonic and coupling with the azimuthal

https://doi.org/10.1017/jfm.2023.333 Published online by Cambridge University Press

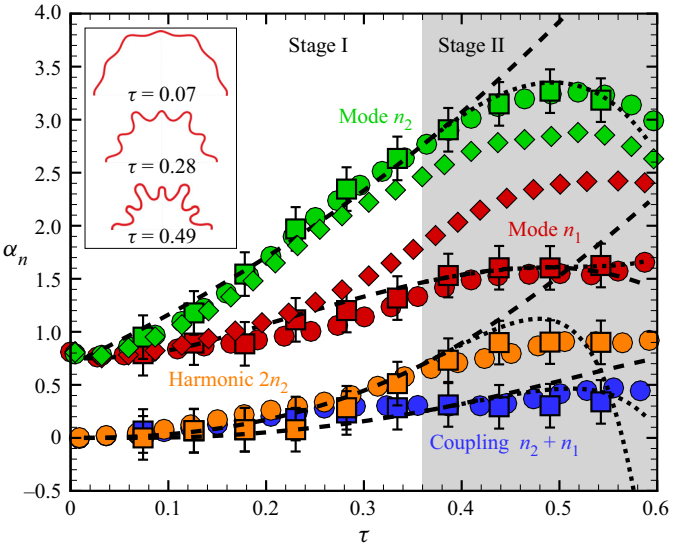

Figure 4. The time-varying dimensionless amplitudes of the two constituent modes (modes n_1 and n_2) and the generated harmonic $2n_1$ and coupling $n_2 + n_1$ obtained from the dual-mode RM instability experiment (square symbols) and simulation (circle symbols). The single-mode RM instabilities of the two constituent modes are numerically calculated and shown with diamond symbols. The dashed lines represent the theoretical predictions in stage I. The dotted lines represent the theoretical predictions in stage II. The inset shows the interfacial contours in the experiment for spectral analysis.

wavenumber n, i.e. a_n, is normalized as $\alpha_n = a_n/a_{n_1}^0$. It can be found that the numerical results quantitatively agree well with the experimental results, further validating the code utilized in the present study.

The amplitude of the mode n_2 is larger than that of the mode n_1 for two reasons. First, according to the linear solution for the cylindrically convergent RM instability on a single-mode interface with a fixed initial amplitude (see (1.2)), the linear amplitude growth rate is larger as n increases. Second, the mode-coupling between modes n_1 and n_2 has a non-negligible influence on the RM instability of the two constituent modes. The amplitude growths of the single-mode RM instability of modes n_1 and n_2 with the same w_0 ($= 3.12$ mm) are numerically calculated, as shown with diamond symbols in figure 4 for comparisons. It is found that the mode-coupling promotes the RM instability of the higher frequency mode (i.e. mode n_2) but suppresses the RM instability of the lower frequency mode (i.e. mode n_1) in the experiment.

The linear solution for the single-mode RM instability (see (1.2)) indicates that the RM instability of each mode is related to the variance of the interface radius. Here, the time-varying interface radius R_i and interface velocity v_i are extracted from the one-dimensional simulation of an unperturbed interface driven by a cylindrically convergent shock using the same initial conditions as the experiment, as shown in figures 5(*a*) and 5(*b*), respectively. It is found that the interface movement can be divided into three stages. Stage I: the interface moves inward uniformly with a speed of Δv during $\tau < 0.36$. Stage II: the interface moves inward with a decreasing velocity during $0.68 > \tau > 0.36$. If we assume that the interface decelerates at a constant acceleration, then the average acceleration ($\bar{g}$) is approximately -1.16×10^6 m s^{-2}. Stage III: the interface is reshocked and moves outward when $\tau > 0.68$. In this study, we focus on the hydrodynamic instabilities of the dual-mode interface in stages I and II.

https://doi.org/10.1017/jfm.2023.333 Published online by Cambridge University Press

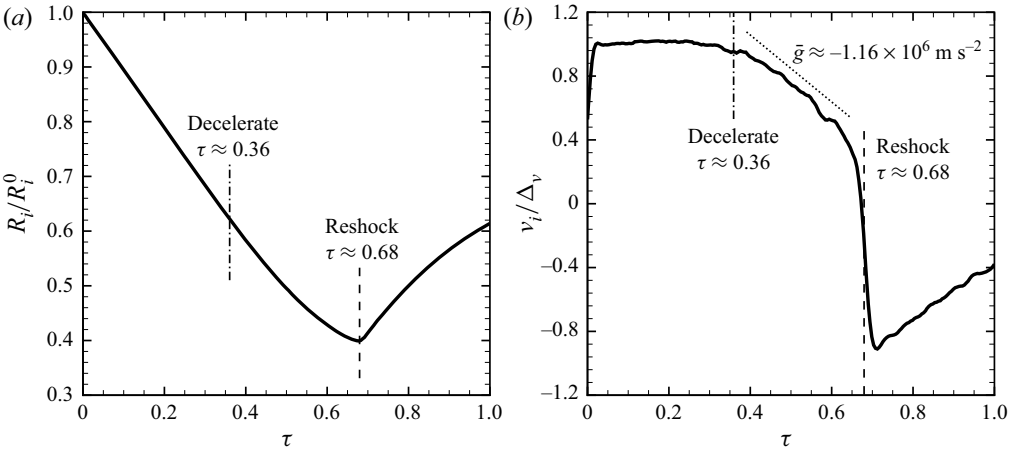

Figure 5. Numerical results on the time-varying dimensionless (*a*) radius and (*b*) velocity of an unperturbed interface driven by a cylindrically convergent shock.

The initial perturbations, potential functions and boundary conditions in the convergent geometry differ from the planar counterpart. As a result, the theoretical models for the convergent multimode RM instability will be quite different from the planar counterpart (Liang *et al.* 2021). Moreover, the evolution of a shocked multimode interface in the planar geometry is only dominated by the RM instability. However, the hydrodynamic instabilities of a shocked multimode interface involve both the RM instability and the additional RT effect. As a result, the theoretical models for the hydrodynamic instabilities in the convergent geometry will be more complicated than the planar geometry and more corresponding to the ICF applications. A series of linear and nonlinear solutions for quantifying the convergent RM instability and additional RT effect will be established in the next step.

4.2. *Linear and weakly nonlinear solutions*

In stage I, the interface motion can be regarded as uniform, and, therefore, the interface radius can be written as $R_i = R_i^0 + \Delta v t$.

Each constituent mode develops linearly at the first-order solution of the RM instability. The first-order linear solutions for the amplitude growth rates of the mode n_1 ($\dot{a}_{n_1}^{RM}$) and mode n_2 ($\dot{a}_{n_2}^{RM}$) can be separately written as

$$\dot{a}_{n_1}^{RM} = \dot{a}_{n_1}^{I} C_r, \quad \dot{a}_{n_2}^{RM} = \dot{a}_{n_2}^{I} C_r, \tag{4.1a,b}$$

where C_r ($\equiv R_i^0/R_i$) represents the convergence ratio and its maximum value in the experiment is 2.5; and $\dot{a}_{n_1}^{I}$ and $\dot{a}_{n_2}^{I}$ represent the initial amplitude growth rates of the mode n_1 and mode n_2 induced by the RM instability, respectively, and which can be calculated as (Mikaelian 2005)

$$\dot{a}_{n_1}^{I} = \frac{a_{n_1}^{+} \Delta v (1 - n_1 A)}{R_i^0}, \quad \dot{a}_{n_2}^{I} = \frac{a_{n_2}^{+} \Delta v (1 - n_2 A)}{R_i^0}, \tag{4.2a,b}$$

in which $a_{n_1}^{+}$ ($= (1 - \Delta v/v_s) a_{n_1}^{0}$) and $a_{n_2}^{+}$ ($= (1 - \Delta v/v_s) a_{n_2}^{0}$) represent the postshock amplitudes of the mode n_1 and mode n_2, respectively. When the initial mixed width

https://doi.org/10.1017/jfm.2023.333 Published online by Cambridge University Press

of the interface w_0 superposed by multiple modes is comparable to the wavelength of the interface and/or the shock intensity is large, the high-amplitude effect and/or the high-Mach-number effect will inhibit the initial amplitude growth rates (Haan 1989; Wouchuk & Nishihara 1997; Rikanati *et al.* 2003; Dell, Stellingwerf & Abarzhi 2015; Campos & Wouchuk 2016; Dell *et al.* 2017). Here, the high-amplitude effect and the high-Mach-number effect on the RM instability are considered independently. Moreover, the startup process before the interface amplitude growth rate reaches the asymptotic value is taken into account. According to Lombardini & Pullin (2009*a*), the characteristic times for the startup processes of the mode n_1 ($t^*_{n_1}$) and mode n_2 ($t^*_{n_2}$) can be evaluated as

$$t^*_{n_1} = \frac{R^0_i}{2n_1}\left[\frac{1+A}{\Delta v + v_f} + \frac{1-A}{\Delta v - v_t}\right], \quad t^*_{n_2} = \frac{R^0_i}{2n_2}\left[\frac{1+A}{\Delta v + v_f} + \frac{1-A}{\Delta v - v_t}\right]. \tag{4.3a,b}$$

Here, we assume that the amplitude growth rates increase linearly from zero to asymptotic values during the startup process.

With the consideration of the high-amplitude effect, the high-Mach-number effect, and the startup process, the expressions of the modified initial amplitude growth rates of the mode n_1 and mode n_2 can be separately rewritten as

$$\dot{a}^I_{n_1} = \frac{HF_{n_1}a^+_{n_1}\Delta v(1-n_1A)f_{n_1}(t)}{R^0_i}, \quad \dot{a}^I_{n_2} = \frac{HF_{n_2}a^+_{n_2}\Delta v(1-n_2A)f_{n_2}(t)}{R^0_i}, \tag{4.4a,b}$$

in which H ($= 1/[1 + (n_{gcd}w_0/6R^0_i)^{(4/3)}]$, with n_{gcd} being the greatest common divisor of n_1 and n_2) is the reduction factor proposed by Dimonte & Ramaprabhu (2010) to quantify the high-amplitude effect; F_{n_1} ($= 1/[1 + \dot{a}^I_{n_1}/(\Delta v - v_t)]$) and F_{n_2} ($= 1/[1 + \dot{a}^I_{n_2}/(\Delta v - v_t)]$) are the reduction factors proposed by Holmes *et al.* (1999) to quantify the high-Mach-number effect on the mode n_1 and mode n_2, respectively; and $f_{n_1}(t)$ and $f_{n_2}(t)$ quantify the startup processes of the mode n_1 and mode n_2, respectively, where $f_{n_1}(t) = t/t^*_{n_1}$ if $t < t^*_{n_1}$ and $f_{n_1}(t) = 1$ if $t \geqslant t^*_{n_1}$, and $f_{n_2}(t) = t/t^*_{n_2}$ if $t < t^*_{n_2}$ and $f_{n_2}(t) = 1$ if $t \geqslant t^*_{n_2}$.

Based on the perturbation expansion method, Guo *et al.* (2014) and Wang *et al.* (2015) separately derived second-order and third-order solutions to quantify the nonlinearity of the RM instability by considering the uniform convergence of a single-mode interface. Here, we rewrite the second-order solutions in the amplitude growth rate form for the harmonic $2n_1$ ($\dot{a}^{RM}_{2n_1}$) and harmonic $2n_2$ ($\dot{a}^{RM}_{2n_2}$) induced by the RM instability as

$$\dot{a}^{RM}_{2n_1} = \frac{a^+_{n_1}\dot{a}^I_{n_1}}{2R_i}(2An_1-1)(C_r-1) + \frac{(\dot{a}^I_{n_1})^2 t}{6R_i}\left[(2An_1-3)C_r^2 - 8An_1C_r\right], \tag{4.5}$$

$$\dot{a}^{RM}_{2n_2} = \frac{a^+_{n_2}\dot{a}^I_{n_2}}{2R_i}(2An_2-1)(C_r-1) + \frac{(\dot{a}^I_{n_2})^2 t}{6R_i}\left[(2An_2-3)C_r^2 - 8An_2C_r\right]. \tag{4.6}$$

Furthermore, Guo, Cheng & Li (2020) extended their previous work (Guo *et al.* 2014) and quantified the mode-coupling effect on the convergent RM instability of the mode n

https://doi.org/10.1017/jfm.2023.333 Published online by Cambridge University Press

at the second-order solution as

$$\frac{\mathrm{d}^2(a_nR_i)}{\mathrm{d}t^2} = (An-3)\frac{\dot{R}_i^2}{R_i^4}\sum_{n'}(a_{n'}R_i)(a_{n''}R_i) - (An+1)\frac{1}{R_i^2}\sum_{n'}\frac{\mathrm{d}(a_{n'}R_i)}{\mathrm{d}t}\frac{\mathrm{d}(a_{n''}R_i)}{\mathrm{d}t} - \frac{1}{R_i^2}\sum_{n'}(a_{n''}R_i)\frac{\mathrm{d}^2(a_{n'}R_i)}{\mathrm{d}t^2} + \frac{\dot{R}_i}{R_i^3}\sum_{n'}\left[(a_{n'}R_i)\frac{\mathrm{d}(a_{n''}R_i)}{\mathrm{d}t} + 3(a_{n''}R_i)\frac{\mathrm{d}(a_{n'}R_i)}{\mathrm{d}t}\right] \tag{4.7}$$

where $n'' = n - n'$. Then, based on (4.7), we can deduce the second-order solutions for the sum and difference couplings, i.e. the amplitude growth rates of the coupling $n_2 + n_1$ ($\dot{a}^{RM}_{n_2+n_1}$) and coupling $n_2 - n_1$ ($\dot{a}^{RM}_{n_2-n_1}$) induced by the RM instability as

$$\dot{a}^{RM}_{n_2+n_1} = \frac{1}{2R_i}(a^+_{n_2}\dot{a}^I_{n_1} + a^+_{n_1}\dot{a}^I_{n_2})\left[A(n_2+n_1)-1\right](C_r-1) + \frac{\dot{a}^I_{n_1}\dot{a}^I_{n_2}t}{3R_i}\left[A(n_2+n_1)(C_r^2-4C_r)-3C_r^2\right], \tag{4.8}$$

$$\dot{a}^{RM}_{n_2-n_1} = \frac{1}{2R_i}\left[A(n_2-n_1)(a^+_{n_2}\dot{a}^{\mathrm{I}}_{n_1} - a^+_{n_1}\dot{a}^I_{n_2}) - (a^+_{n_1}\dot{a}^I_{n_2} + a^+_{n_2}\dot{a}^I_{n_1})\right](C_r-1) + \frac{\dot{a}^I_{n_1}\dot{a}^I_{n_2}t}{3R_i}\left[A(n_2-n_1)(C_r^2+2C_r)-3C_r^2\right]. \tag{4.9}$$

The first sum terms on the right-hand side of (4.5), (4.6), (4.8) and (4.9) represent the time-independent linear amplitude growth rates of harmonics $2n_1$, harmonics $2n_2$, couplings $n_2 + n_1$ and couplings $n_2 - n_1$, respectively. The second sum terms on the right-hand side of (4.5), (4.6), (4.8) and (4.9) represent the time-dependent weakly nonlinear modifications on the growth rates of harmonics $2n_1$, harmonics $2n_2$, couplings $n_2 + n_1$ and couplings $n_2 - n_1$, respectively. The first sum terms indicate that the nonlinearity of the convergent RM instability and the mode-coupling between the two initially constituent modes separately generate new harmonics and couplings from the very beginning, especially when the amplitudes of constituent modes are large, which coincides with our previous study on the multimode RM instability in the planar geometry (Liang *et al.* 2021).

Notably, the feedback of harmonics and couplings to the modes having the same wavenumber influences the RM instability of the initially constituent modes. For example, since $n_2 = 2n_1$ in the experiment, the RM instability of the mode n_1 consists of the amplitude of the mode n_1 at the first-order solution and the amplitude of the coupling $n_2 - n_1$ at the second-order solution; and the RM instability of the mode n_2 consists of the amplitude of the mode n_2 at the first-order solution and the amplitude of the harmonics $2n_1$ at the second-order solution. The theoretical predictions for the time-varying amplitudes of modes n_1 and n_2, the harmonic $2n_2$ and the coupling $n_2 + n_1$ are calculated using (4.1*a*,*b*), (4.4*a*,*b*)–(4.6) and (4.8)–(4.9), as shown with dashed lines in figure 4. It is found that the theoretical predictions agree well with the experimental and numerical results before the interface decelerates ($\tau < 0.36$). When the interface begins to decelerate, the additional RT effect is superimposed on the interface, and, therefore, the theoretical predictions deviate from the experimental and numerical results. For example, the

https://doi.org/10.1017/jfm.2023.333 Published online by Cambridge University Press

theoretical predictions obviously overestimate the amplitudes of modes and harmonics with large wavenumbers (e.g. mode n_2 and harmonics $2n_2$).

In stage II, the interface decelerates with an average acceleration $\bar{g}$ and can be approximately written as $R_i = R_i^0 + \Delta v t - \frac{1}{2}\bar{g}(t - t^d)^2$, with t^d being the time when the interface begins to decelerate. We only consider the mode-coupling between the two initially modes since the amplitudes of modes n_1 and n_2 are much larger than the generated harmonics and couplings. Similarly, due to the nonlinearity of the RT instability (Jacobs & Catton 1988; Wang *et al.* 2013; Liu *et al.* 2020), modes n_1 and n_2 also generate two harmonics with wavenumbers $2n_1$ and $2n_2$, respectively. Moreover, the mode-coupling between modes n_1 and n_2 also generates two couplings with wavenumbers $n_2 + n_1$ and $n_2 - n_1$ (Haan 1989, 1991; Ofer *et al.* 1992).

Wang *et al.* (2013) studied the linear solution for quantifying the time-varying amplitude growth of mode n at a constant acceleration. Here, the first-order linear solutions for the mode n_1 ($\dot{a}_{n_1}^{RT}$), mode n_2 ($\dot{a}_{n_2}^{RT}$), harmonic $2n_2$ ($\dot{a}_{2n_2}^{RT}$) and coupling $n_2 - n_1$ ($\dot{a}_{n_2-n_1}^{RT}$) induced by the additional RT effect at a constant acceleration can be rewritten in the amplitude growth rate form as

$$\left.\begin{aligned}
\dot{a}_{n_1}^{RT} &= -\gamma_{n_1} a_{n_1}^{RM}(t^d)\sinh(\gamma_{n_1} t^{\xi}),\\
\dot{a}_{n_2}^{RT} &= -\gamma_{n_2} a_{n_2}^{RM}(t^d)\sinh(\gamma_{n_2} t^{\xi}),\\
\dot{a}_{2n_2}^{RT} &= -\gamma_{2n_2} a_{2n_2}^{RM}(t^d)\sinh(\gamma_{2n_2} t^{\xi}),\\
\dot{a}_{n_2-n_1}^{RT} &= -\gamma_{n_2-n_1} a_{n_2-n_1}^{RM}(t^d)\sinh(\gamma_{n_2-n_1} t^{\xi}),
\end{aligned}\right\} \tag{4.10}$$

in which $t^{\xi} = t - t^d$; $\gamma_{n_1} = \sqrt{A\bar{g}n_1/R_i}$, $\gamma_{n_2} = \sqrt{A\bar{g}n_2/R_i}$, $\gamma_{2n_2} = \sqrt{2A\bar{g}n_2/R_i}$ and $\gamma_{n_2-n_1} = \sqrt{A\bar{g}(n_2 - n_1)/R_i}$ are the linear growth rates of the mode n_1, mode n_2, harmonic $2n_2$ and coupling $n_2 - n_1$ caused by the additional RT effect, respectively; and $a_{n_1}^{RM}(t^d)$, $a_{n_2}^{RM}(t^d)$, $a_{2n_2}^{RM}(t^d)$ and $a_{n_2-n_1}^{RM}(t^d)$ are the amplitudes of the mode n_1, mode n_2, harmonic $2n_2$ and coupling $n_2 - n_1$ at the moment t^d, respectively, and which can be calculated by the nonlinear solutions in stage I.

Based on the perturbation expansion method, Guo *et al.* (2018) derived an analytical, second-order solution for the RT instability under a constant acceleration. We rewrite the second-order solutions in the amplitude growth rate form for the harmonic $2n_1$ ($\dot{a}_{2n_1}^{RT}$) and harmonic $2n_2$ ($\dot{a}_{2n_2}^{RT}$) caused by the additional RT effect as

$$\begin{aligned}
\dot{a}_{2n_1}^{RT} = {} & \frac{[a_{n_1}^{RM}(t^d)]^2}{2R_i}[4(An_1+1)\gamma_1\sinh(\gamma_1 t^{\xi})\cosh(\gamma_1 t^{\xi})\\
& -(2An_1+1)\gamma_{2n_1}\sinh(\gamma_{2n_1} t^{\xi})],
\end{aligned} \tag{4.11}$$

$$\begin{aligned}
\dot{a}_{2n_2}^{RT} = {} & \frac{[a_{n_2}^{RM}(t^d)]^2}{2R_i}[4(An_2+1)\gamma_2\sinh(\gamma_2 t^{\xi})\cosh(\gamma_2 t^{\xi})\\
& -(2An_2+1)\gamma_{2n_2}\sinh(\gamma_{2n_2} t^{\xi})].
\end{aligned} \tag{4.12}$$

Furthermore, the mode-coupling effect on the RT instability was considered by Guo (2018). We rewrite the second-order solutions in the amplitude growth rate form for the coupling $n_2 + n_1$ ($\dot{a}_{n_2+n_1}^{RT}$) and coupling $n_2 - n_1$ ($\dot{a}_{n_2-n_1}^{RT}$) caused by the additional RT

https://doi.org/10.1017/jfm.2023.333 Published online by Cambridge University Press

effect as

$$\dot{a}^{RT}_{n_2+n_1} = \frac{[a^{RM}_{n_1}(t^d)][a^{RM}_{n_2}(t^d)]}{2R_i}\left\{\frac{n_2+n_1}{2\sqrt{n_1 n_2}}[\gamma_{n_1}\cosh(\gamma_{n_1}t^{\xi})\sinh(\gamma_{n_2}t^{\xi}) + \gamma_{n_2}\sinh(\gamma_{n_1}t^{\xi})\cosh(\gamma_{n_2}t^{\xi})] + [1+A(n_2+n_1)][\gamma_{n_1}\sinh(\gamma_{n_1}t^{\xi})\cosh(\gamma_{n_2}t^{\xi}) + \gamma_{n_2}\cosh(\gamma_{n_1}t^{\xi})\sinh(\gamma_{n_2}t^{\xi}) - \gamma_{n_2+n_1}\sinh(\gamma_{n_2+n_1}t^{\xi})]\right\}, \tag{4.13}$$

$$\dot{a}^{RT}_{n_2-n_1} = \frac{[a^{RM}_{n_1}(t^d)][a^{RM}_{n_2}(t^d)]}{4R_i}\left\{\sqrt{\frac{n_2}{n_1}}[\gamma_{n_1}\cosh(\gamma_{n_1}t^{\xi})\sinh(\gamma_{n_2}t^{\xi}) + \gamma_{n_2}\sinh(\gamma_{n_1}t^{\xi})\cosh(\gamma_{n_2}t^{\xi})] + [1-2A(n_2-n_1)][\gamma_{n_1}\sinh(\gamma_{n_1}t^{\xi})\cosh(\gamma_{n_2}t^{\xi}) + \gamma_{n_2}\cosh(\gamma_{n_1}t^{\xi})\sinh(\gamma_{n_2}t^{\xi}) - \gamma_{n_2-n_1}\sinh(\gamma_{n_2-n_1}t^{\xi})]\right\}. \tag{4.14}$$

The theoretical predictions of the amplitude growths of modes, harmonics and couplings with the same wavenumbers in stage II are calculated by the nonlinear solutions of the RM instability ((4.1*a*,*b*), (4.4*a*,*b*)–(4.6) and (4.8)–(4.9)) plus the nonlinear solutions of the additional RT effect (4.10)–(4.14), as shown with dotted lines in figure 4. The theoretical predictions show a better agreement with the experimental and numerical results of the hydrodynamic instabilities of modes n_1 and n_2 and the coupling n_2+n_1 than the instabilities of the harmonic $2n_2$. There are two possible reasons for the poor prediction of the harmonic $2n_2$. On the one hand, as the azimuthal wavenumber n increases, the nonlinearity caused by high-order (third-order and greater) harmonics more influences the instability, and, therefore, the predictions with second-accuracy on the additional RT effect gradually lose their accuracy. On the other hand, we simplify the interface movement in stage II with a constant acceleration, which is different from the actual interface motion with a time-varying acceleration. Since the geometry convergence plays a more important role in the additional RT effect as n increases, the predictions assuming a constant acceleration gradually lose their accuracy. Nevertheless, the theoretical predictions capture the most significant features, i.e. the first-order instabilities of the two constituted modes and the second-order feedback from harmonics and couplings to the modes.

Moreover, compared with the prediction that only considers the convergent RM instability, it is found that the additional RT effect suppresses the instabilities of the mode n_2, harmonic $2n_2$ and coupling n_2+n_1 but promotes the instabilities of the mode n_1. This conclusion is different from the convergent RM instability on a single-mode air–SF_6 interface that the additional RT effect always suppresses instability (Ding *et al.* 2017*a*; Lei *et al.* 2017; Vandenboomgaerde *et al.* 2018*b*; Luo *et al.* 2018, 2019), indicating that the mode-coupling complicates the hydrodynamic instabilities of a multimode interface, even resulting in different outcomes of the additional RT effect on the multimode interface and single-mode interface.

4.3. *Parametric analysis*

In the second-order solutions for the convergent RM instability and additional RT effect, it is evident that when the wavenumber of one constituent mode of a dual-mode interface is twice the wavenumber of the other constituent mode, the generated second-order harmonics and couplings influence the amplitude growth rates of the two constituent modes since the coupling n_2-n_1 applies the feedback to the mode n_1, and the harmonic

https://doi.org/10.1017/jfm.2023.333 Published online by Cambridge University Press

Case	n_1	n_2	a_1^0 (mm)	a_2^0 (mm)	w_0 (mm)	δ
IPδ0.25	6	12	1.0	0.125	2.00	0.25
IPδ0.50	6	12	1.0	0.25	2.00	0.50
IPδ1.0	6	12	1.0	0.50	2.25	1.0
IPδ2.0	6	12	1.0	1.0	3.12	2.0
IPδ4.0	6	12	1.0	2.0	5.06	4.0
APδ-0.25	6	12	1.0	−0.125	2.00	−0.25
APδ-0.50	6	12	1.0	−0.25	2.00	−0.50
APδ-1.0	6	12	1.0	−0.50	2.25	−1.0
APδ-2.0	6	12	1.0	−1.0	3.12	−2.0
APδ-4.0	6	12	1.0	−2.0	5.06	−4.0

Table 1. The initial spectrum parameters of the two constituent modes of a dual-mode interface in numerical simulations: n_1 and n_2 denote the azimuthal wavenumbers of the two constituent modes; a_1^0 and a_2^0 denote the initial amplitudes of the mode n_1 and mode n_2, respectively; w_0 denotes the initial mixed width of the dual-mode interface; δ $(= n_2 a_2^0 / n_1 a_1^0)$ denotes the ratio of the amplitude-to-wavelength ratios of the two constituent modes.

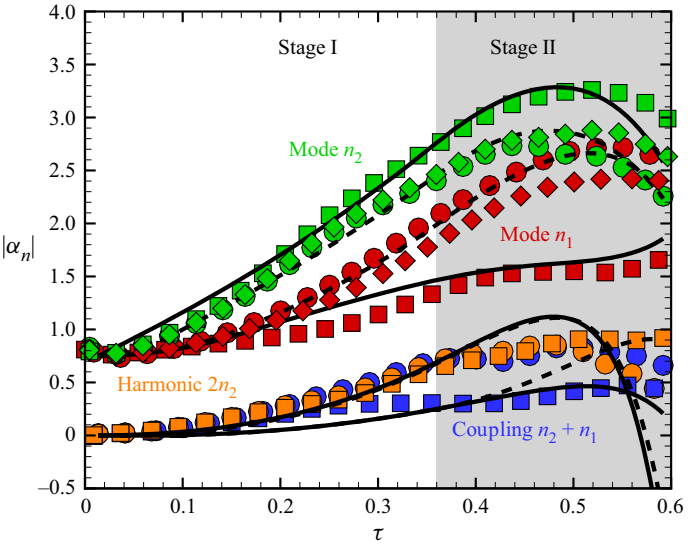

Figure 6. Comparisons of the dimensionless amplitudes of the two constituent modes (modes n_1 and n_2) and the generated harmonic $2n_2$ and coupling $n_2 + n_1$ obtained from the simulations in cases IPδ2.0 (square symbols) and APδ-2.0 (circle symbols), where the single-mode RM instabilities of the two constituent modes are shown with diamond symbols. The solid and dashed lines represent the theoretical predictions for cases IPδ2.0 and APδ-2.0, respectively.

$2n_1$ imposes the feedback on the mode n_2. In the experiment, we only consider a specific case where the perturbations on the two constituent modes are inphase, and the ratio of the amplitude-to-wavelength ratios of the two constituent modes δ $(= n_2 a_2^0 / n_1 a_1^0)$ equals 2.0. However, the initial perturbations on the surfaces in applications are random. Therefore, the perturbations on the two constituent modes might be antiphase, and δ should be various. Numerical simulations on a dual-mode air–SF_6 interface having the same gas physics parameters as the experiment, but different spectra with the experiment, are performed to investigate the influences of relative phases and δ on the hydrodynamic instabilities of a dual-mode interface in the cylindrical geometry. The initial spectrum parameters in different cases are listed in table 1.

https://doi.org/10.1017/jfm.2023.333 Published online by Cambridge University Press

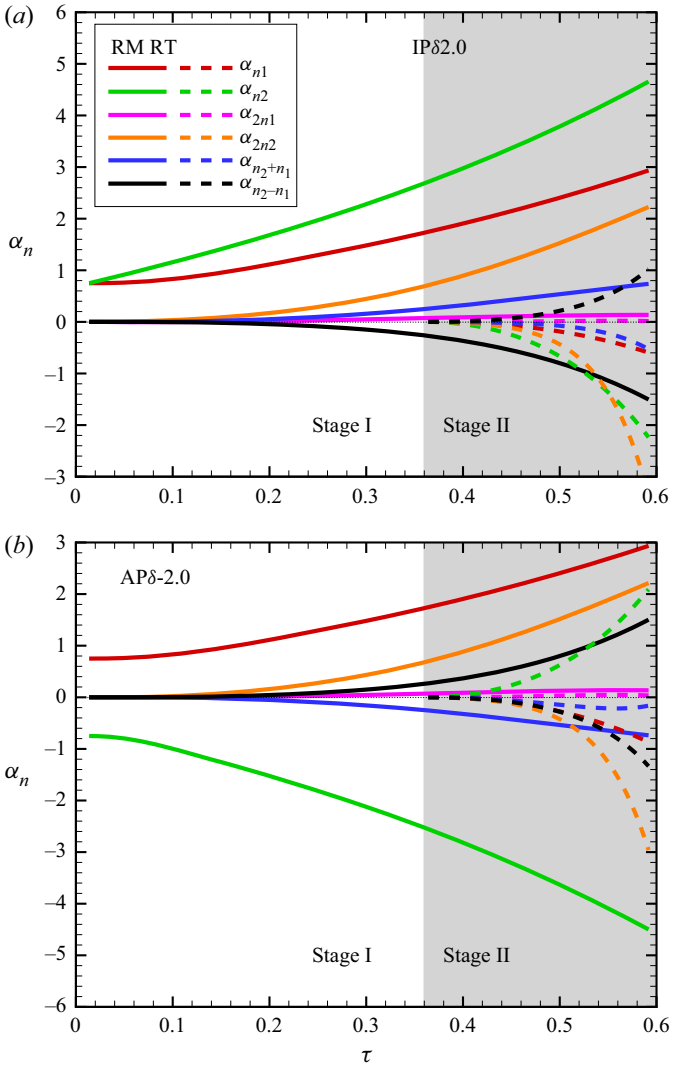

Figure 7. Comparisons of the dimensionless amplitudes of modes, harmonics and couplings predicted by theories in cases (*a*) IPδ2.0 and (*b*) APδ-2.0. Solid and dashed lines represent the theoretical predictions for the RM instability and the additional RT effect, respectively.

First, the influences of the phase difference between the two constituent modes on the hydrodynamic instabilities are explored by comparing cases IPδ2.0 and APδ-2.0, as shown in figure 6. Compared with the amplitude growths of single-mode interfaces, the mode-coupling slightly promotes the lower frequency mode (i.e. mode n_1) but slightly suppresses the higher frequency mode (i.e. mode n_2) in the APδ-2.0 case, which is different from the IPδ2.0 case, indicating that the phase difference influences the mode-coupling. Moreover, it is found that the amplitude growth of the coupling $n_2 + n_1$ in the antiphase case is larger than the inphase case. In addition, the theoretical predictions of the two constituent modes and two generated harmonics in cases IPδ2.0 and APδ-2.0 are shown with solid and dashed lines, and which agree well with the numerical results, further validating the nonlinear solutions.

https://doi.org/10.1017/jfm.2023.333 Published online by Cambridge University Press

The theoretical predictions for the RM instability and the additional RT effect of all modes, harmonics and couplings in cases IPδ2.0 and APδ-2.0 are shown in figures 7(a) and 7(b), respectively. In stage I, the influence of the phase difference on the RM instability is considered. It is evident that the RM unstable perturbation of the coupling $n_2 - n_1$ grows in the opposite (or same) direction to the RM unstable perturbation of the mode n_1 in the IPδ2.0 (or APδ-2.0) case. Meanwhile, the RM unstable perturbation of the harmonic $2n_1$ grows in the same (or opposite) direction with the RM unstable perturbation of the mode n_2 in the IPδ2.0 (or APδ-2.0) case. Therefore, the generated coupling $n_2 - n_1$ suppresses the instability of the mode n_1; whereas, the generated harmonic $2n_1$ promotes the instability of the mode n_2 when the two constituent modes are inphase. Oppositely, the generated coupling $n_2 - n_1$ promotes the instability of the mode n_1; whereas, the generated harmonic $2n_1$ suppresses the instability of the mode n_2 when the two constituent modes are antiphase.

In stage II, the influence of the phase difference on the additional RT effect is considered. It is evident that the RT unstable perturbation of the coupling $n_2 - n_1$ grows in the same (or opposite) direction to the RT unstable perturbation of the mode n_1 in the IPδ2.0 (or APδ-2.0) case. Meanwhile, the RT unstable perturbation of the harmonic $2n_1$ grows in the same (or opposite) direction with the RT unstable perturbation of the mode n_2 in the IPδ2.0 (or APδ-2.0) case. Therefore, the generated coupling $n_2 - n_1$ and harmonic $2n_1$ separately promote the instabilities of the mode n_1 and mode n_2 when the two constituent modes are inphase. And the generated coupling $n_2 - n_1$ and harmonic $2n_1$ separately suppress the instabilities of the mode n_1 and mode n_2 when the two constituent modes are antiphase. However, in the IPδ2.0 case, the RT unstable perturbation of the coupling $n_2 - n_1$ is larger than that of the mode n_1, therefore, the instabilities of the mode n_1 are promoted by the additional RT effect on comparing with the pure RM instability; whereas, the RT unstable perturbation of the harmonic $2n_1$ is smaller than that of the mode n_2, therefore, the instabilities of the mode n_2 are suppressed by the additional RT effect on comparing with the pure RM instability.

Moreover, the sign of the perturbation of the coupling $n_2 + n_1$ induced by the additional RT effect is the same as that induced by the RM instability in the IPδ2.0 case. Differently, the sign of the perturbation of the coupling $n_2 + n_1$ induced by the additional RT effect is opposite to that induced by the RM instability in the APδ-2.0 case. Therefore, the amplitude growths of the coupling $n_2 + n_1$ in the antiphase case are larger than the inphase case.

Overall, the phase difference influences the mode-coupling mechanism, resulting in different feedbacks of the generated second-order harmonics and couplings to the initially constituent modes, leading to different outcomes of the RM instability and additional RT effect.

Second, the influences of δ on the instability developments of the two constituent modes are numerically investigated. The initial amplitude of the mode n_1 is fixed as 1.0 mm. The initial amplitudes of the mode n_2 vary from 0.125 mm to 2.0 mm in the five inphase cases and -0.125 mm to -2.0 mm in the five antiphase cases. The initial interface contours in various cases are shown in figure 8. The dual-mode interface's crests and troughs in inphase cases are the troughs and crests in corresponding antiphase cases. As $|\delta|$ increases, the differences of the initial interface contours in corresponding inphase and antiphase cases are more pronounced. The time-varying dimensionless amplitudes of the two constituent modes in the five inphase cases and five antiphase cases are obtained from numerical simulations, as shown in figures 9(a) and 9(b), respectively.

https://doi.org/10.1017/jfm.2023.333 Published online by Cambridge University Press

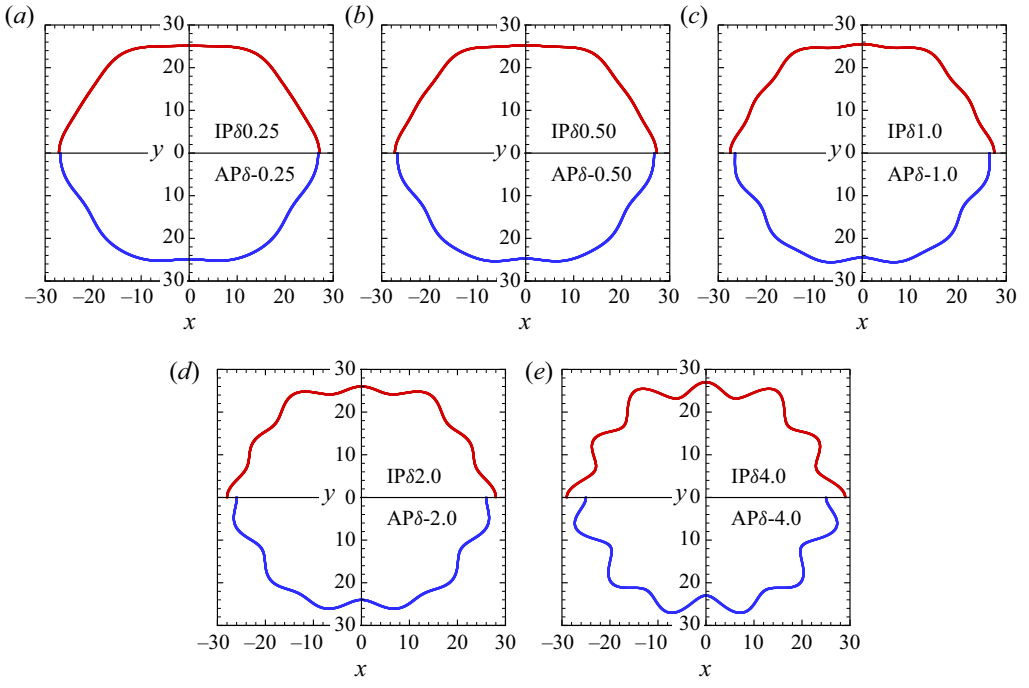

Figure 8. Initial interface contours corresponding to cases (*a*) IPδ0.25 and APδ-0.25, (*b*) IPδ0.50 and APδ-0.50, (*c*) IPδ1.0 and APδ-1.0, (*d*) IPδ2.0 and APδ-2.0 and (*e*) IPδ4.0 and APδ-4.0.

In the five inphase cases, as δ increases, due to the increasing negative feedback of the coupling $n_2 - n_1$ and the increasing suppression introduced by the high-amplitude effect, the amplitude growth of the mode n_1 is more suppressed. As δ increases, due to the decreasing positive feedback of the harmonic $2n_1$ and the increasing suppression introduced by the high-amplitude effect, the amplitude growth of the mode n_1 is more suppressed.

In the five antiphase cases, as $|\delta|$ increases from 0.25 to 1.0 (or 1.0 to 4.0), the positive feedback of the coupling $n_2 - n_1$ is larger (or less) than the suppression introduced by the high-amplitude effect, therefore, the amplitude growth of the mode n_1 is more promoted (or suppressed). Differently, as $|\delta|$ increases from 0.25 to 1.0 (or 1.0 to 4.0), the decreasing negative feedback of the harmonic $2n_1$ is more (or less) significant than the increasing high-amplitude effect, therefore, the amplitude growth of the mode n_2 is more promoted (or suppressed).

Overall, the competition between the mode-coupling effect and the high-amplitude effect varies as δ changes, resulting in different outcomes of the RM instability and additional RT effect. It is also noted that the lower frequency mode is largely suppressed when the two constituent modes are inphase and δ is large, and the higher frequency mode is largely suppressed when the two constituent modes are antiphase and $|\delta|$ is small. In addition, the theoretical predictions of the hydrodynamic instabilities of the mode n_1 and mode n_2 are shown with solid and dashed lines with colours corresponding to symbols, which agree well with the numerical results, further validating the generality of the nonlinear solutions.

Last, the mixed mass and normalized mixed mass of a convergent dual-mode RM unstable interface are calculated using numerical simulations. The actual amount of mixed

https://doi.org/10.1017/jfm.2023.333 Published online by Cambridge University Press

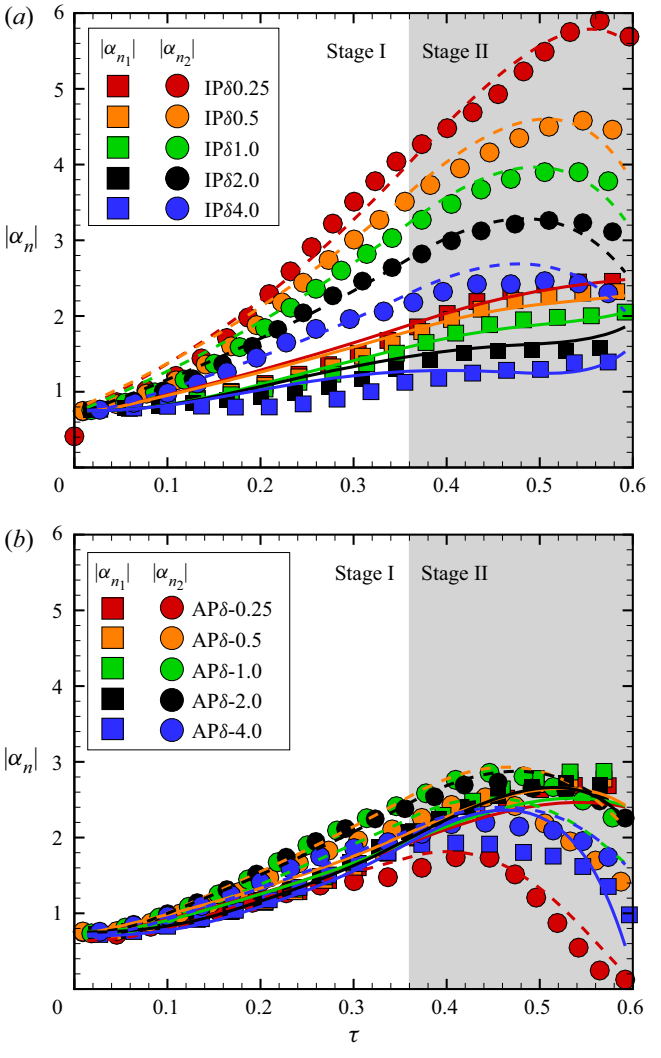

Figure 9. Comparisons of the dimensionless amplitudes of the mode n_1 (square symbols) and mode n_2 (circle symbols) obtained from numerical simulations in the (*a*) inphase cases and (*b*) antiphase cases. The solid and dashed lines with colours corresponding to the symbols represent the theoretical predictions for the mode n_1 and mode n_2, respectively.

mass could be viewed as a more direct indicator of the evolution of the mixing layers. Zhou, Cabot & Thornber (2016) studied the mixed mass of a slow/fast RM unstable interface in the planar geometry and pointed out that an especially attractive feature of the mixed mass is that it is a conserved quantity. To frame the characterization based on how much the heavy fluid is mixed into the light fluid, the mixed mass M measurement can be defined as

$$M = \int 4\rho Y_1 Y_2 \, \mathrm{d}V, \tag{4.15}$$

where Y_1 and Y_2 are the mass fractions of the heavy fluid and light fluid, respectively; ρ is the mixture density; and V is the volume that encloses the mixing region. Since the surrounding gas is air and the test gas is a mixture of air and SF_6, and the mass fraction

https://doi.org/10.1017/jfm.2023.333 Published online by Cambridge University Press

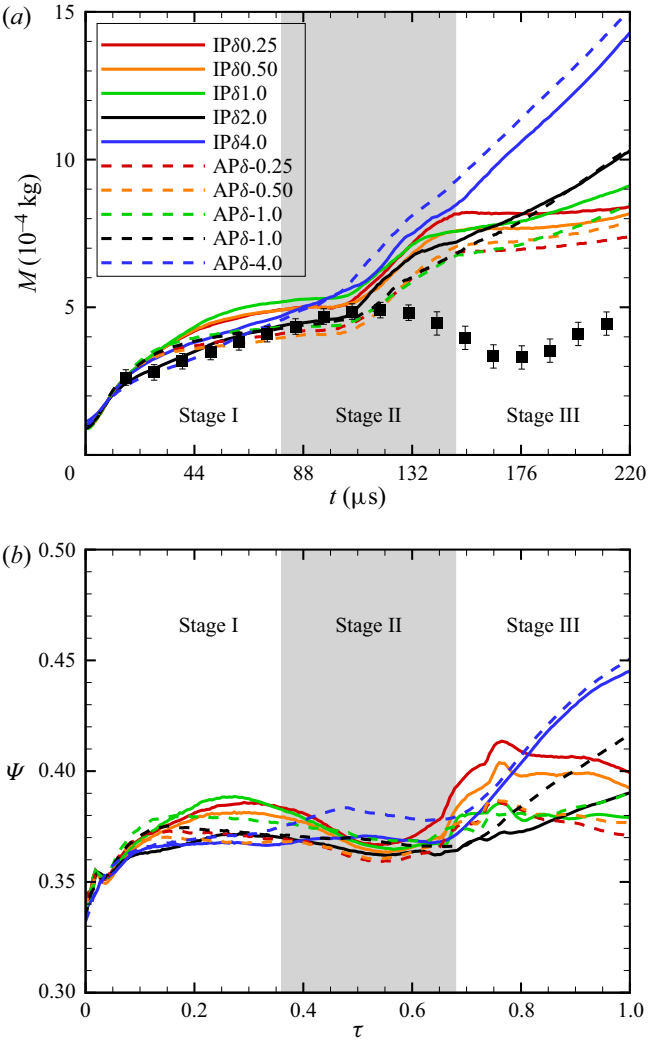

Figure 10. Temporal evolutions of the (*a*) mixed mass M (lines) and (*b*) normalized mixed mass Ψ obtained from numerical simulations. The experimental results for the mixed width (symbols) in (*a*) are multiplied by arbitrary constants.

of SF_6 in the test gas is 91.1 % in the present study, the maximum and minimum values of Y_1 are 91.1 % and 0, respectively; and the maximum and minimum values of Y_2 are 100 % and 8.9 %, respectively. Figure 10(*a*) shows the temporal evolution of the mixed mass obtained from numerical simulations in various cases (solid lines). We also present the corresponding experimental results for the mixed width (symbols) in the case IPδ2.0 multiplied by arbitrary constants. Clearly, before the negative growth of the mixed width in stage II (approximately 110 s, dimensionless time 0.5), the mixed mass measurements closely track the scaling of the mixed width, which is the same as the planar RT and RM instabilities (Zhou *et al.* 2016) and the cylindrical RT instability (Zhao *et al.* 2021). However, the amount of mixed mass of a convergent RM unstable interface shows a rapid increase due to the flow's increasing density as the transmitted shock converges at the geometric centre. As a result, the mixed mass curves of the convergent RM instability

https://doi.org/10.1017/jfm.2023.333 Published online by Cambridge University Press

coupled with the additional RT effect differ from the planar RT instability (Zhou *et al.* 2016), RM instability (Mohaghar *et al.* 2019; Zhou, Groom & Thornber 2020*a*; Bender *et al.* 2021) and the cylindrical RT instability (Zhao *et al.* 2021). We also compare the mixed mass of a dual-mode interface in various cases considering different initial spectra, as shown in figure 10(*a*). It is found that the mixed mass of the dual-mode interface in the inphase cases is slightly larger than the corresponding antiphase cases before the additional RT effect causes a quicker increase of the mixed mass. After the additional RT effect and reshock dominate the flow instability, the mixed mass shows different growth trends in various cases, indicating that the transition mixing of a convergent dual-mode interface depends on the initial spectrum.

The normalized mixed mass is given by

$$\Psi = \frac{\int \rho Y_1 Y_2 \,\mathrm{d}V}{\int \langle\rho\rangle\langle Y_1\rangle\langle Y_2\rangle \,\mathrm{d}V}, \tag{4.16}$$

where $\langle\rangle$ denotes the spatial average in the x–y plane. The normalized mixed mass expresses a ratio of subzonal mixing to larger-scale entrainment, describing the time evolution of how effectively the mass of the materials have been mixed within the mixing layer (Zhou *et al.* 2016; Bender *et al.* 2021). The normalized mixed mass of the convergent RM unstable interface in various cases is shown in figure 10(*b*). First, after the incident shock impacts the interface, as smaller-scale structures develop and physical and numerical dissipation ensues, Ψ gradually rises, especially when δ is small. Then, the additional RT effect suppresses the development of the Ψ in stage II, finally with a rapid increase of the Ψ due to reshock in stage III. The differences of Ψ in various cases are enlarged by the reshock. In summary, the initial spectrum of a dual-mode interface has a non-negligible influence on the mixing evolution.

5. Conclusions

Experiments are performed for the first time on the convergent RM instability of a dual-mode interface in a shock-tube facility, and the perturbation growth of each Fourier mode is measured. The dual-mode air–SF_6 interface is created by an extended soap-film technique in the semiannular shock tube facility. Precise interfacial morphologies and wave patterns are captured by high-speed schlieren photography. For the first time, the influences of the mode-coupling on the convergent RM instability coupled with the RT effect of all modes, harmonics and couplings from linear to nonlinear stages are theoretically quantified with second-order nonlinear solutions. Numerical simulations solving compressible Euler equations are also performed considering various initial spectra. The temporal evolutions of the mixed mass and normalized mixed mass of a shocked multimode interface are calculated for the first time to quantify the mixing of two fluids in cylindrical geometry.

The amplitude growths of the initially constituent modes and the second-order harmonics and their couplings are obtained by a serial Fourier analysis of the interfacial contours extracted from the schlieren images. A noticeable difference between the growths of the constituent modes and the corresponding single-mode RM instability is observed, suggesting the evident mode-coupling effect on the convergent dual-mode RM instability. A series of analytical, nonlinear solutions with second-order accuracy are adopted by considering the geometry convergence, the mode-coupling mechanism, the

https://doi.org/10.1017/jfm.2023.333 Published online by Cambridge University Press

high-amplitude effect, the high-Mach-number effect and the startup process to quantify the RM instability and the additional RT effect on the dual-mode interface. The nonlinear solutions well predict the amplitude growths of the first-order modes and the second-order harmonics and couplings before the reshock in the experiment and simulations. The mode-coupling complicates the hydrodynamic instabilities of a multimode interface, even resulting in different outcomes of the additional RT effect on the multimode interface and single-mode interface.

Referring to the nonlinear solutions, it is evident that when the azimuthal wavenumber of one constituent mode is twice the azimuthal wavenumber of the other constituent mode of a dual-mode interface, the mode-coupling has a non-negligible influence on the hydrodynamic instabilities of the two constituent modes. Based on the theory and simulations, it is proved that the phase difference and the ratio of the amplitude-to-wavelength ratios of the two constituent modes δ greatly influence the mode-coupling mechanism. For a dual-mode interface consisting of inphase (or antiphase) modes n and $2n$, the mode-coupling suppresses (or promotes) the instability of the mode n but promotes (or suppresses) the instability of the mode $2n$. Moreover, as δ varies, the competition between the mode-coupling effect and the high-amplitude effect complicates the hydrodynamic instabilities of the constituent modes. For a dual-mode interface, the lower frequency mode is largely suppressed when the two constituent modes are inphase and δ is large, and the higher frequency mode is largely suppressed when the two constituent modes are antiphase and $|\delta|$ is small.

Last, the time-varying mixed mass and normalized mixed mass of the convergent RM unstable interface under various initial conditions are calculated using numerical simulations. It is found that the mixed mass shows a rapid increase due to the flow's density increment when the transmitted shock converges. The mixed mass curves of the convergent RM instability coupled with the additional RT effect differ from the planar RT and RM instabilities and the cylindrical RT instability. The additional RT effect suppresses, but the reshock promotes the growth of the normalized mixed mass of the convergent RM unstable interface. The initial spectrum has a non-negligible influence on the mixed mass and normalized mixed mass variations.

Overall, the hydrodynamic instabilities of a multimode interface driven by a convergent shock closely depend on the initial spectra from the very beginning. The mode-coupling mechanism revealed in the convergent dual-mode RM instability and additional RT effect would be of great use for understanding and modelling the hydrodynamic instabilities of a multimode interface consisting of random waves. We believe it is an essential step towards the elaborate study of the turbulence driven by a convergent shock.

In further studies, we will use a new quantitative experimental technique, e.g. planar laser-induced fluorescence/particle image velocimetry (Mohaghar *et al.* 2017, 2019; Mohaghar 2019; Noble *et al.* 2020; Noble 2022) and direct numerical simulations to enhance our understanding of the physics of the flow for the convergent multimode RM instability, and in general to enhance our understanding of the RM instability and the additional RT effect. The unanswered question is how the convergent multimode RM and RT instabilities can develop into turbulence with different initial conditions at later stages, which is directly related to the ICF performance.

Funding. This work was supported by Tamkeen under the NYU Abu Dhabi Research Institute grant CG002, the Natural Science Foundation of China (nos. 91952205 and 11625211) and Hong Kong Research Grants Council (no. 15207420).

Declaration of interests. The authors report no conflict of interest.

https://doi.org/10.1017/jfm.2023.333 Published online by Cambridge University Press

Author ORCIDs.
Yu Liang https://orcid.org/0000-0002-3254-7073;
Xisheng Luo https://orcid.org/0000-0002-4303-8290;
Chih-Yung Wen https://orcid.org/0000-0002-1181-8786.

References

Abarzhi, S.I. 2008 Coherent structures and pattern formation in Rayleigh–Taylor turbulent mixing. *Phys. Scr.* **78** (1), 015401.

Abarzhi, S.I. 2010 Review of theoretical modelling approaches of Rayleigh–Taylor instabilities and turbulent mixing. *Phil. Trans. R. Soc. Lond.* A **368** (1916), 1809–1828.

Abgrall, R. 1996 How to prevent pressure oscillations in multicomponent flow calculations: a quasi conservative approach. *J. Comput. Phys.* **125** (1), 150–160.

Alon, U., Hecht, J., Mukamel, D. & Shvarts, D. 1994 Scale invariant mixing rates of hydrodynamically unstable interface. *Phys. Rev. Lett.* **72**, 2867–2870.

Alon, U., Hecht, J., Ofer, D. & Shvarts, D. 1995 Power laws and similarity of Rayleigh–Taylor and Richtmyer–Meshkov mixing fronts. *Phys. Rev. Lett.* **74**, 534–537.

Amendt, P., Colvin, J.D., Ramshaw, J.D., Robey, H.F. & Landen, O.L. 2003 Modified Bell–Plesset effect with compressibility: application to double-shell ignition target designs. *Phys. Plasmas* **10** (3), 820–829.

Apazidis, N. & Lesser, M.B. 1996 On generation and convergence of polygonal-shaped shock waves. *J. Fluid Mech.* **309**, 301–319.

Apazidis, N., Lesser, M.B., Tillmark, N. & Johansson, B. 2002 An experimental and theoretical study of converging polygonal shock waves. *Shock Waves* **12**, 39–58.

Balasubramanian, S., Orlicz, G.C. & Prestridge, K.P. 2013 Experimental study of initial condition dependence on turbulent mixing in shock-accelerated Richtmyer–Meshkov fluid layers. *J. Turbul.* **14** (3), 170–196.

Bates, J.W. 2004 Initial value problem solution for isolated rippled shock fronts in arbitrary fluid media. *Phys. Rev.* E **69** (5), 056313.

Bell, G.I. 1951 Taylor instability on cylinders and spheres in the small amplitude approximation. *Tech. Rep.* LA-1321. Los Alamos National Laboratory.

Bender, J.D., *et al*. 2021 Simulation and flow physics of a shocked and reshocked high-energy-density mixing layer. *J. Fluid Mech.* **915**, A84.

Biamino, L., Jourdan, G., Houas, L., Vandenboomgaerde, M. & Souffland, D. 2017 Light/heavy converging Richtmyer–Meshkov instability in a conventional shock tube. In *International Symposium on Shock Waves* (ed. A. Sasoh, T. Aoki & M. Katayama), pp. 595–601. Springer.

Biamino, L., Jourdan, G., Mariani, C., Houas, L., Vandenboomgaerde, M. & Souffland, D. 2015 On the possibility of studying the converging Richtmyer–Meshkov instability in a conventional shock tube. *Exp. Fluids* **56**, 26.

Brasseur, M., Vandenboomgaerde, M., Mariani, C., Barros, D.C., Souffland, D. & Jourdan, G. 2021 Experimental generation of spherical converging shock waves. *Exp. Fluids* **62** (7), 1–8.

Brouillette, M. 2002 The Richtmyer–Meshkov instability. *Annu. Rev. Fluid Mech.* **34**, 445–468.

Campos, F.C. & Wouchuk, J.G. 2016 Analytical scalings of the linear Richtmyer–Meshkov instability when a shock is reflected. *Phys. Rev.* E **93** (5), 053111.

Chester, W. 1954 The quasi-cylindrical shock tube. *Phil. Mag.* **45**, 1293–1301.

Chisnell, R.F. 1957 The motion of a shock wave in a channel, with applications to cylindrical and spherical shock waves. *J. Fluid Mech.* **2**, 286–298.

Dell, Z., Stellingwerf, R.F. & Abarzhi, S.I. 2015 Effect of initial perturbation amplitude on Richtmyer–Meshkov flows induced by strong shocks. *Phys. Plasmas* **22** (9), 092711.

Dell, Z.R., Pandian, A., Bhowmick, A.K., Swisher, N.C., Stanic, M., Stellingwerf, R.F. & Abarzhi, S.I. 2017 Maximum initial growth-rate of strong-shock-driven Richtmyer–Meshkov instability. *Phys. Plasmas* **24** (9), 090702.

Di Stefano, C.A., Malamud, G., Kuranz, C.C., Klein, S.R. & Drake, R.P. 2015*a* Measurement of Richtmyer–Meshkov mode coupling under steady shock conditions and at high energy density. *High Energy Density Phys.* **17**, 263–269.

Di Stefano, C.A., Malamud, G., Kuranz, C.C., Klein, S.R., Stoeckl, C. & Drake, R.P. 2015*b* Richtmyer–Meshkov evolution under steady shock conditions in the high-energy-density regime. *Appl. Phys. Lett.* **106** (11), 114103.

https://doi.org/10.1017/jfm.2023.333 Published online by Cambridge University Press

DIMONTE, G. & RAMAPRABHU, P. 2010 Simulations and model of the nonlinear Richtmyer–Meshkov instability. *Phys. Fluids* **22**, 014104.

DIMONTE, G. & SCHNEIDER, M. 2000 Density ratio dependence of Rayleigh–Taylor mixing for sustained and impulsive acceleration histories. *Phys. Fluids* **12**, 304–321.

DIMOTAKIS, P.E. & SAMTANEY, R. 2006 Planar shock cylindrical focusing by a perfect-gas lens. *Phys. Fluids* **18**, 031705.

DING, J., DENG, X. & LUO, X. 2021 Convergent Richtmyer–Meshkov instability on a light gas layer with perturbed inner and outer surfaces. *Phys. Fluids* **33** (10), 102112.

DING, J., LI, J., SUN, R., ZHAI, Z. & LUO, X. 2019 Convergent Richtmyer–Meshkov instability of a heavy gas layer with perturbed outer interface. *J. Fluid Mech.* **878**, 277–291.

DING, J., LIANG, Y., CHEN, M., ZHAI, Z., SI, T. & LUO, X. 2018 Interaction of planar shock wave with three-dimensional heavy cylindrical bubble. *Phys. Fluids* **30** (10), 106109.

DING, J., SI, T., YANG, J., LU, X., ZHAI, Z. & LUO, X. 2017*a* Measurement of a Richtmyer–Meshkov instability at an air-SF_6 interface in a semiannular shock tube. *Phys. Rev. Lett.* **119** (1), 014501.

DING, J.C., SI, T., CHEN, M.J., ZHAI, Z.G., LU, X.Y. & LUO, X.S. 2017*b* On the interaction of a planar shock with a three-dimensional light gas cylinder. *J. Fluid Mech.* **828**, 289–317.

DRAKE, R.P. 2018 *High-Energy-Density Physics: Foundation of Inertial Fusion and Experimental Astrophysics*. Springer.

ELBAZ, Y. & SHVARTS, D. 2018 Modal model mean field self-similar solutions to the asymptotic evolution of Rayleigh–Taylor and Richtmyer–Meshkov instabilities and its dependence on the initial conditions. *Phys. Plasmas* **25** (6), 062126.

EPSTEIN, R. 2004 On the Bell–Plesset effects: the effects of uniform compression and geometrical convergence on the classical Rayleigh–Taylor instability. *Phys. Plasmas* **11** (11), 5114–5124.

FAN, E., GUAN, B., WEN, C.Y. & SHEN, H. 2019 Numerical study on the jet formation of simple-geometry heavy gas inhomogeneities. *Phys. Fluids* **31**, 026103.

FINCKE, J.R., LANIER, N.E., BATHA, S.H., HUECKSTAEDT, R.M., MAGELSSEN, G.R., ROTHMAN, S.D., PARKER, K.W. & HORSFIELD, C.J. 2004 Postponement of saturation of the Richtmyer–Meshkov instability in a convergent geometry. *Phys. Rev. Lett.* **93** (11), 115003.

GLENDINNING, S.G., *et al*. 2000 Ablation front Rayleigh–Taylor growth experiments in spherically convergent geometry. *Phys. Plasmas* **7** (5), 2033–2039.

GROOM, M. & THORNBER, B. 2020 The influence of initial perturbation power spectra on the growth of a turbulent mixing layer induced by Richtmyer–Meshkov instability. *Physica* D **407**, 132463.

GROVE, J.W., HOLMES, R., SHARP, D.H., YANG, Y. & ZHANG, Q. 1993 Quantitative theory of Richtmyer–Meshkov instability. *Phys. Rev. Lett.* **71**, 3473–3476.

GUAN, B., LIU, Y., WEN, C.-Y. & SHEN, H. 2018 Numerical study on liquid droplet internal flow under shock impact. *AIAA J.* **56** (9), 3382–3387.

GUO, H. 2018 Theoretical study of weakly nonlinear Rayleigh–Taylor instability in cylindrical implosions. PhD thesis, China Academy of Engineering Physics.

GUO, H., CHENG, T. & LI, Y. 2020 Weakly nonlinear multi-mode Bell–Plesset growth in cylindrical geometry. *Chin. Phys.* B **29** (11), 115202.

GUO, H., WANG, L., YE, W., WU, J. & ZHANG, W. 2018 Weakly nonlinear Rayleigh–Taylor instability in cylindrically convergent geometry. *Chin. Phys. Lett.* **35** (5), 055201.

GUO, H., YU, X., WANG, L., YE, W., WU, J. & LI, Y. 2014 On the second harmonic generation through Bell–Plesset effects in cylindrical geometry. *Chin. Phys. Lett.* **31** (4), 044702.

GUO, X., CONG, Z., SI, T. & LUO, X. 2022 Shock-tube studies of single- and quasi-single-mode perturbation growth in Richtmyer–Meshkov flows with reshock. *J. Fluid Mech.* **941**, A65.

HAAN, S.W. 1989 Onset of nonlinear saturation for Rayleigh–Taylor growth in the presence of a full spectrum of modes. *Phys. Rev.* A **39** (11), 5812.

HAAN, S.W. 1991 Weakly nonlinear hydrodynamic instabilities in inertial fusion. *Phys. Fluids* B **3**, 2349–2355.

HERRMANN, M., MOIN, P. & ABARZHI, S.I. 2008 Nonlinear evolution of the Richtmyer–Meshkov instability. *J. Fluid Mech.* **612**, 311–338.

HOLMES, R.L., DIMONTE, G., FRYXELL, B., GITTINGS, M.L., GROVE, J.W., SCHNEIDER, M., SHARP, D.H., VELIKOVICH, A.L., WEAVER, R.P. & ZHANG, Q. 1999 Richtmyer–Meshkov instability growth: experiment, simulation and theory. *J. Fluid Mech.* **389**, 55–79.

HOLMES, R.L. & GROVE, J.W. 1995 Numerical investigation of Richtmyer–Meshkov instability using front tracking. *J. Fluid Mech.* **301**, 51–64.

HOSSEINI, S.H.R. & TAKAYAMA, K. 2005 Experimental study of Richtmyer–Meshkov instability induced by cylndrical shock waves. *Phys. Fluids* **17**, 084101.

https://doi.org/10.1017/jfm.2023.333 Published online by Cambridge University Press

IGRA, D. & IGRA, O. 2020 Shock wave interaction with a polygonal bubble containing two different gases, a numerical investigation. *J. Fluid Mech.* **889**, A26.

JACOBS, J.W. & CATTON, I. 1988 Three-dimensional Rayleigh–Taylor instability. Part 1. Weakly nonlinear theory. *J. Fluid Mech.* **187**, 329–352.

JIANG, Y., WEN, C.-Y. & ZHANG, D. 2020 Space-time conservation element and solution element method and its applications. *AIAA J.* **58** (12), 5408–5430.

KJELLANDER, M., TILLMARK, N. & APAZIDIS, N. 2012 Energy concentration by spherical converging shocks generated in a shock tube. *Phys. Fluids* **24** (12), 126103.

LEI, F., DING, J., SI, T., ZHAI, Z. & LUO, X. 2017 Experimental study on a sinusoidal air/SF_6 interface accelerated by a cylindrically converging shock. *J. Fluid Mech.* **826**, 819–829.

LEINOV, E., MALAMUD, G., ELBAZ, Y., LEVIN, L.A., BEN-DOR, G., SHVARTS, D. & SADOT, O. 2009 Experimental and numerical investigation of the Richtmyer–Meshkov instability under re-shock conditions. *J. Fluid Mech.* **626**, 449–475.

LI, J., DING, J., LUO, X. & ZOU, L. 2022 Instability of a heavy gas layer induced by a cylindrical convergent shock. *Phys. Fluids* **34** (4), 042123.

LI, J., DING, J., SI, T. & LUO, X. 2020*a* Convergent Richtmyer–Meshkov instability of light gas layer with perturbed outer surface. *J. Fluid Mech.* **884**, R2.

LI, M., DING, J., ZHAI, Z., SI, T., LIU, N., HUANG, S. & LUO, X. 2020*b* On divergent Richtmyer–Meshkov instability of a light/heavy interface. *J. Fluid Mech.* **901**, A38.

LI, X., FU, Y., YU, C. & LI, L. 2021 Statistical characteristics of turbulent mixing in spherical and cylindrical converging Richtmyer–Meshkov instabilities. *J. Fluid Mech.* **928**, A10.

LIANG, Y. 2022*a* *Fundamental Studies of Shock-Driven Hydrodynamic Instabilities*. Springer Nature.

LIANG, Y. 2022*b* The phase effect on the Richtmyer–Meshkov instability of a fluid layer. *Phys. Fluids* **34** (3), 034106.

LIANG, Y., DING, J., ZHAI, Z., SI, T. & LUO, X. 2017 Interaction of cylindrically converging diffracted shock with uniform interface. *Phys. Fluids* **29** (8), 086101.

LIANG, Y., LIU, L. & LUO, X. 2022 Experimental study of bubble competition and spike competition in Richtmyer–Meshkov flows. *J. Fluid Mech.* **949**, A3.

LIANG, Y., LIU, L., ZHAI, Z., DING, J., SI, T. & LUO, X. 2021 Richtmyer–Meshkov instability on two-dimensional multi-mode interfaces. *J. Fluid Mech.* **928**, A37.

LIANG, Y. & LUO, X. 2023 Hydrodynamic instabilities of two successive slow/fast interfaces induced by a weak shock. *J. Fluid Mech.* **955**, A40.

LIANG, Y., ZHAI, Z., DING, J. & LUO, X. 2019 Richtmyer–Meshkov instability on a quasi-single-mode interface. *J. Fluid Mech.* **872**, 729–751.

LIANG, Y., ZHAI, Z. & LUO, X. 2018 Interaction of strong converging shock wave with SF_6 gas bubble. *Sci. China Phys. Mech.* **61** (6), 1–9.

LIANG, Y., ZHAI, Z., LUO, X. & WEN, C.-Y. 2020 Interfacial instability at a heavy/light interface induced by rarefaction waves. *J. Fluid Mech.* **885**, A42.

LIU, H. & XIAO, Z. 2016 Scale-to-scale energy transfer in mixing flow induced by the Richtmyer–Meshkov instability. *Phys. Rev.* E **93** (5), 053112.

LIU, L., LIANG, Y., DING, J., LIU, N. & LUO, X. 2018 An elaborate experiment on the single-mode Richtmyer–Meshkov instability. *J. Fluid Mech.* **853**, R2.

LIU, W., HE, X. & YU, C. 2012 Cylindrical effects on Richtmyer–Meshkov instability for arbitrary Atwood numbers in weakly nonlinear regime. *Phys. Plasmas* **19** (7), 072108.

LIU, W., WANG, X., LIU, X., YU, C., FANG, M. & YE, W. 2020 Pure single-mode Rayleigh–Taylor instability for arbitrary Atwood numbers. *Sci. Rep.* **10** (1), 1–9.

LIU, W., YU, C., YE, W., WANG, L. & HE, X. 2014 Nonlinear theory of classical cylindrical Richtmyer–Meshkov instability for arbitrary Atwood numbers. *Phys. Plasmas* **21** (6), 062119.

LIVERTS, M. & APAZIDIS, N. 2016 Limiting temperatures of spherical shock wave implosion. *Phys. Rev. Lett.* **116**, 014501.

LIVESCU, D. 2020 Turbulence with large thermal and compositional density variations. *Annu. Rev. Fluid Mech.* **52**, 309–341.

LOMBARDINI, M. & PULLIN, D.I. 2009*a* Startup process in the Richtmyer–Meshkov instability. *Phys. Fluids* **21** (4), 044104.

LOMBARDINI, M. & PULLIN, D.I. 2009*b* Small-amplitude perturbations in the three-dimensional cylindrical Richtmyer–Meshkov instability. *Phys. Fluids* **21**, 114103.

LOMBARDINI, M., PULLIN, D.I. & MEIRON, D.I. 2014 Turbulent mixing driven by spherical implosions. Part 1. Flow description and mixing-layer growth. *J. Fluid Mech.* **748**, 85.

https://doi.org/10.1017/jfm.2023.333 Published online by Cambridge University Press

Luo, X., Ding, J., Wang, M., Zhai, Z. & Si, T. 2015 A semi-annular shock tube for studying cylindrically converging Richtmyer–Meshkov instability. *Phys. Fluids* **27** (9), 091702.
Luo, X., Li, M., Ding, J., Zhai, Z. & Si, T. 2019 Nonlinear behaviour of convergent Richtmyer–Meshkov instability. *J. Fluid Mech.* **877**, 130–141.
Luo, X., Liu, L., Liang, Y., Ding, J. & Wen, C.-Y. 2020 Richtmyer–Meshkov instability on a dual-mode interface. *J. Fluid Mech.* **905**, A5.
Luo, X., Si, T., Yang, J. & Zhai, Z. 2014 A cylindrical converging shock tube for shock-interface studies. *Rev. Sci. Instrum.* **85**, 015107.
Luo, X., Zhang, F., Ding, J., Si, T., Yang, J., Zhai, Z. & Wen, C. 2018 Long-term effect of Rayleigh–Taylor stabilization on converging Richtmyer–Meshkov instability. *J. Fluid Mech.* **849**, 231–244.
Mansoor, M.M., Dalton, S.M., Martinez, A.A., Desjardins, T., Charonko, J.J. & Prestridge, K.P. 2020 The effect of initial conditions on mixing transition of the Richtmyer–Meshkov instability. *J. Fluid Mech.* **904**, A3.
Matsuoka, C. & Nishihara, K. 2006 Fully nonlinear evolution of a cylindrical vortex sheet in incompressible Richtmyer–Meshkov instabilitys. *Phys. Rev.* E **73**, 055304.
Meshkov, E.E. 1969 Instability of the interface of two gases accelerated by a shock wave. *Fluid Dyn.* **4**, 101–104.
Mikaelian, K.O. 1990 Rayleigh–Taylor and Richtmyer–Meshkov instabilities and mixing in stratified spherical shells. *Phys. Rev.* A **42**, 3400.
Mikaelian, K.O. 2005 Rayleigh–Taylor and Richtmyer–Meshkov instabilities and mixing in stratified cylindrical shells. *Phys. Fluids* **17**, 094105.
Miles, A.R. 2004 Bubble merger model for the nonlinear Rayleigh–Taylor instability driven by a strong blast wave. *Phys. Plasmas* **11**, 5140–5155.
Miles, A.R., Edwards, M.J., Blue, B., Hansen, J.F., Robey, H.F., Drake, R.P., Kuranz, C. & Leibrandt, D.R. 2004 The effects of a short-wavelength mode on the evolution of a long-wavelength perturbatoin driven by a strong blast wave. *Phys. Plasmas* **11**, 5507–5519.
Mohaghar, M. 2019 Effects of initial conditions and Mach number on turbulent mixing transition of shock-driven variable-density flow. PhD thesis, Georgia Institute of Technology.
Mohaghar, M., Carter, J., Musci, B., Reilly, D., McFarland, J.A. & Ranjan, D. 2017 Evaluation of turbulent mixing transition in a shock-driven variable-density flow. *J. Fluid Mech.* **831**, 779–825.
Mohaghar, M., Carter, J., Pathikonda, G. & Ranjan, D. 2019 The transition to turbulence in shock-driven mixing: effects of Mach number and initial conditions. *J. Fluid Mech.* **871**, 595–635.
Niederhaus, C.E. & Jacobs, J.W. 2003 Experimental study of the Richtmyer–Meshkov instability of incompressible fluids. *J. Fluid Mech.* **485**, 243–277.
Niederhaus, J.H.J., Greenough, J.A., Oakley, J.G., Ranjan, D., Anderson, M.H. & Bonazza, R. 2008 A computational parameter study for the three-dimensional shock-bubble interaction. *J. Fluid Mech.* **594**, 85–124.
Nishihara, K., Wouchuk, J.G., Matsuoka, C., Ishizaki, R. & Zhakhovsky, V.V. 2010 Richtmyer–Meshkov instability: theory of linear and nonlinear evolution. *Phil. Trans. R. Soc. Lond.* A **368**, 1769–1807.
Noble, C.D. 2022 High-speed measurements of mixing due to the Richtmyer–Meshkov instability in a twice-shocked gas interface. PhD thesis, The University of Wisconsin-Madison.
Noble, C.D., Herzog, J.M., Ames, A.M., Oakley, J., Rothamer, D.A. & Bonazza, R. 2020 High speed PLIF study of the Richtmyer–Meshkov instability upon re-shock. *Physica* D **410**, 132519.
Ofer, D., Alon, U., Shvarts, D., McCrory, R.L. & Verdon, C.P. 1996 Modal model for the nonlinear multimode Rayleigh–Taylor instability. *Phys. Plasmas* **3** (8), 3073–3090.
Ofer, D., Shvarts, D., Zinamon, Z. & Orszag, S.A. 1992 Mode coupling in nonlinear Rayleigh–Taylor instability. *Phys. Fluids* B **4** (11), 3549–3561.
Oron, D., Arazi, L., Kartoon, D., Rikanati, A., Alon, U. & Shvarts, D. 2001 Dimensionality dependence of the Rayleigh–Taylor and Richtmyer–Meshkov instability late-time scaling laws. *Phys. Plasmas* **8**, 2883–2889.
Pandian, A., Stellingwerf, R.F. & Abarzhi, S.I. 2017 Effect of a relative phase of waves constituting the initial perturbation and the wave interference on the dynamics of strong-shock-driven Richtmyer–Meshkov flows. *Phys. Rev. Fluids* **2** (7), 073903.
Peterson, J.L., Casey, D.T., Hurricane, O.A., Raman, K.S., Robey, H.F. & Smalyuk, V.A. 2015 Validating hydrodynamic growth in National Ignition Facility implosions. *Phys. Plasmas* **22** (5), 056309.
Plesset, M.S. 1954 On the stability of fluid flows with spherical symmetry. *J. Appl. Phys.* **25**, 96–98.
Quirk, J.J. & Karni, S. 1996 On the dynamics of a shock-bubble interaction. *J. Fluid Mech.* **318**, 129–163.

https://doi.org/10.1017/jfm.2023.333 Published online by Cambridge University Press

RAYLEIGH, LORD 1883 Investigation of the character of the equilibrium of an incompressible heavy fluid of variable density. *Proc. Lond. Math. Soc.* **14**, 170–177.

REMINGTON, B.A., WEBER, S.V., MARINAK, M.M., HAAN, S.W., KILKENNY, J.D., WALLACE, R.J. & DIMONTE, G. 1995 Single-mode and multimode Rayleigh–Taylor experiments on nova. *Phys. Plasmas* **2** (1), 241–255.

RICHTMYER, R.D. 1960 Taylor instability in shock acceleration of compressible fluids. *Commun. Pure Appl. Maths* **13**, 297–319.

RIKANATI, A., ALON, U. & SHVARTS, D. 1998 Vortex model for the nonlinear evolution of the multimode Richtmyer–Meshkov instability at low Atwood numbers. *Phys. Rev.* E **58**, 7410–7418.

RIKANATI, A., ORON, D., SADOT, O. & SHVARTS, D. 2003 High initial amplitude and high Mach number effects on the evolution of the single-mode Richtmyer–Meshkov instability. *Phys. Rev.* E **67**, 026307.

SADOT, O., EREZ, L., ALON, U., ORON, D., LEVIN, L.A., EREZ, G., BEN-DOR, G. & SHVARTS, D. 1998 Study of nonlinear evolution of single-mode and two-bubble interaction under Richtmyer–Meshkov instability. *Phys. Rev. Lett.* **80**, 1654–1657.

SEMBIAN, S. & LIVERTS, M. 2020 On using converging shock waves for pressure amplification in shock tubes. *Metrologia* **57** (3), 035008.

SEMBIAN, S., LIVERTS, M. & APAZIDIS, N. 2018 Plane blast wave interaction with an elongated straight and inclined heat-generated inhomogeneity. *J. Fluid Mech.* **851**, 245–267.

SHEN, H. & PARSANI, M. 2017 The role of multidimensional instabilities in direct initiation of gaseous detonations in free space. *J. Fluid Mech.* **813**, R4.

SHEN, H. & WEN, C.-Y. 2016 A characteristic space-time conservation element and solution element method for conservation laws. II. Multidimensional extension. *J. Comput. Phys.* **305** (C), 775–792.

SHEN, H., WEN, C.-Y., LIU, K.X. & ZHANG, D.L. 2015*a* Robust high-order space-time conservative schemes for solving conservation laws on hybrid meshes. *J. Comput. Phys.* **281**, 375–402.

SHEN, H., WEN, C.Y., PARSANI, M. & SHU, C.W. 2017 Maximum-principle-satisfying space-time conservation element and solution element scheme applied to compressible multifluids. *J. Comput. Phys.* **330**, 668–692.

SHEN, H., WEN, C.-Y. & ZHANG, D.L. 2015*b* A characteristic space-time conservation element and solution element method for conservation laws. *J. Comput. Phys.* **288**, 101–118.

SHYUE, K.M. 1998 An efficient shock-capturing algorithm for compressible multicomponent problems. *J. Comput. Phys.* **142** (1), 208–242.

SI, T., LONG, T., ZHAI, Z. & LUO, X. 2015 Experimental investigation of cylindrical converging shock waves interacting with a polygonal heavy gas cylinder. *J. Fluid Mech.* **784**, 225–251.

SI, T., ZHAI, Z. & LUO, X. 2014*a* Experimental study of Richtmyer–Meshkov instability in a cylindrical converging shock tube. *Laser Part. Beams* **32**, 343–351.

SI, T., ZHAI, Z., LUO, X. & YANG, J. 2014*b* Experimental study on a heavy-gas cylinder accelerated by cylindrical converging shock waves. *Shock Waves* **24**, 3–9.

SMALYUK, V.A., *et al*. 2014 First measurements of hydrodynamic instability growth in indirectly driven implosions at ignition-relevant conditions on the national ignition facility. *Phys. Rev. Lett.* **112** (18), 185003.

SREBRO, Y., ELBAZ, Y., SADOT, O., ARAZI, L. & SHVARTS, D. 2003 A general buoyancy-drag model for the evolution of the Rayleigh–Taylor and Richtmyer–Meshkov instabilities. *Laser Part. Beams* **21**, 347–353.

SUN, R., DING, J., ZHAI, Z., SI, T. & LUO, X. 2020 Convergent Richtmyer–Meshkov instability of heavy gas layer with perturbed inner surface. *J. Fluid Mech.* **902**, A3.

TANG, J., ZHANG, F., LUO, X. & ZHAI, Z. 2021 Effect of atwood number on convergent Richtmyer–Meshkov instability. *Acta Mechanica Sin.* **37** (3), 434–446.

TAYLOR, G. 1950 The instability of liquid surfaces when accelerated in a direction perpendicular to their planes. I. *Proc. R. Soc. Lond.* A **201** (1065), 192–196.

THORNBER, B. 2016 Impact of domain size and statistical errors in simulations of homogeneous decaying turbulence and the Richtmyer–Meshkov instability. *Phys. Fluids* **28** (4), 045106.

THORNBER, B., DRIKAKIS, D., YOUNGS, D.L. & WILLIAMS, R.J.R. 2010 The influence of initial condition on turbulent mixing due to Richtmyer–Meshkov instability. *J. Fluid Mech.* **654**, 99–139.

THORNBER, B., *et al*. 2017 Late-time growth rate, mixing, and anisotropy in the multimode narrowband Richtmyer–Meshkov instability: the θ-group collaboration. *Phys. Fluids* **29** (10), 105107.

TORO, E.F., SPRUCE, M. & SPEARES, W. 1994 Restoration of the contact surface in the HLL-Riemann solver. *Shock Waves* **4** (1), 25–34.

TUBBS, D.L., BARNES, C.W., BECK, J.B., HOFFMAN, N.M., OERTEL, J.A., WATT, R.G., BOEHLY, T., BRADLEY, D., JAANIMAGI, P. & KNAUER, J. 1999 Cylindrical implosion experiments using laser direct drive. *Phys. Plasmas* **6** (5), 2095–2104.

https://doi.org/10.1017/jfm.2023.333 Published online by Cambridge University Press

VANDENBOOMGAERDE, M., GAUTHIER, S. & MÜGLER, C. 2002 Nonlinear regime of a multimode Richtmyer–Meshkov instability: a simplified perturbation theory. *Phys. Fluids* **14** (3), 1111–1122.

VANDENBOOMGAERDE, M., ROUZIER, P., SOUFFLAND, D., BIAMINO, L., JOURDAN, G., HOUAS, L. & MARIANI, C. 2018*a* Nonlinear growth of the converging Richtmyer–Meshkov instability in a conventional shock tube. *Phys. Rev. Fluids* **3**, 014001.

VANDENBOOMGAERDE, M., ROUZIER, P., SOUFFLAND, D., MARIANI, C., BIAMINO, L., JOURDAN, G. & HOUAS, L. 2018*b* Experimental, numerical and theoretical investigation of the converging Richtmyer–Meshkov instability in a conventional shock tube. In *16th International Workshop on the Physics of Compressible Turbulent Mixing*.

VELIKOVICH, A.L. & DIMONTE, G. 1996 Nonlinear perturbation theory of the incompressible Richtmyer–Meshkov instability. *Phys. Rev. Lett.* **76** (17), 3112.

WANG, L., WU, J., GUO, H., YE, W., LIU, J., ZHANG, W. & HE, X. 2015 Weakly nonlinear Bell–Plesset effects for a uniformly converging cylinder. *Phys. Plasmas* **22** (8), 082702.

WANG, L.F., WU, J.F., YE, W.H., ZHANG, W.Y. & HE, X.T. 2013 Weakly nonlinear incompressible Rayleigh–Taylor instability growth at cylindrically convergent interfaces. *Phys. Plasmas* **20**, 042708.

WHITHAM, G.B. 1958 On the propagation of shock waves through regions of non-uniform area or flow. *J. Fluid Mech.* **4**, 337–360.

WOUCHUK, J.G. & NISHIHARA, K. 1997 Asymptotic growth in the linear Richtmyer–Meshkov instability. *Phys. Plasmas* **4** (4), 1028–1038.

WU, J., LIU, H. & XIAO, Z. 2021 Refined modelling of the single-mode cylindrical Richtmyer–Meshkov instability. *J. Fluid Mech.* **908**, A9.

YAN, Z., FU, Y., WANG, L., YU, C. & LI, X. 2022 Effect of chemical reaction on mixing transition and turbulent statistics of cylindrical Richtmyer–Meshkov instability. *J. Fluid Mech.* **941**, A55.

ZHAI, Z., LI, W., SI, T., LUO, X., YANG, J. & LU, X. 2017 Refraction of cylindrical converging shock wave at an air/helium gaseous interface. *Phys. Fluids* **29** (1), 016102.

ZHAI, Z., LIANG, Y., LIU, L., DING, J., LUO, X. & ZOU, L. 2018*a* Interaction of rippled shock wave with flat fast-slow interface. *Phys. Fluids* **30** (4), 046104.

ZHAI, Z., LIU, C., QIN, F., YANG, J. & LUO, X. 2010 Generation of cylindrical converging shock waves based on shock dynamcis theory. *Phys. Fluids* **22**, 041701.

ZHAI, Z., OU, J. & DING, J. 2019*a* Coupling effect on shocked double-gas cylinder evolution. *Phys. Fluids* **31** (9), 096104.

ZHAI, Z., SI, T., LUO, X., YANG, J., LIU, C., TAN, D. & ZOU, L. 2012 Parametric study of cylindrical converging shock waves generated based on shock dynamics theory. *Phys. Fluids* **24**, 026101.

ZHAI, Z., ZHANG, F., ZHOU, Z., DING, J. & WEN, C.-Y. 2019*b* Numerical study on Rayleigh–Taylor effect on cylindrically converging Richtmyer–Meshkov instability. *Sci. China Phys. Mech.* **62** (12), 1–10.

ZHAI, Z., ZOU, L., WU, Q. & LUO, X. 2018*b* Review of experimental Richtmyer–Meshkov instability in shock tube: from simple to complex. *Proc. Inst. Mech. Engrs* **232**, 2830–2849.

ZHANG, Q. & GRAHAM, M.J. 1997 Scaling laws for unstable interfaces driven by strong shocks in cylindrical geometry. *Phys. Rev. Lett.* **79**, 2674–2677.

ZHANG, Q. & GRAHAM, M.J. 1998 A numerical study of Richtmyer–Meshkov instability driven by cylindrical shocks. *Phys. Fluids* **10**, 974–992.

ZHANG, Q. & SOHN, S.I. 1997 Nonlinear theory of unstable fluid mixing driven by shock wave. *Phys. Fluids* **9**, 1106–1124.

ZHAO, Z., WANG, P., LIU, N. & LU, X. 2021 Scaling law of mixing layer in cylindrical Rayleigh–Taylor turbulence. *Phys. Rev.* E **104** (5), 055104.

ZHOU, Y. 2017*a* Rayleigh–Taylor and Richtmyer–Meshkov instability induced flow, turbulence, and mixing. I. *Phys. Rep.* **720-722**, 1–136.

ZHOU, Y. 2017*b* Rayleigh–Taylor and Richtmyer–Meshkov instability induced flow, turbulence, and mixing. II. *Phys. Rep.* **723–725**, 1–160.

ZHOU, Y., CABOT, W.H. & THORNBER, B. 2016 Asymptotic behavior of the mixed mass in Rayleigh–Taylor and Richtmyer–Meshkov instability induced flows. *Phys. Plasmas* **23** (5), 052712.

ZHOU, Y., CLARK, T.T., CLARK, D.S., GLENDINNING, S.S., SKINNER, A.A., HUNTINGTON, C., HURRICANE, O.A., DIMITS, A.M. & REMINGTON, B.A. 2019 Turbulent mixing and transition criteria of flows induced by hydrodynamic instabilities. *Phys. Plasmas* **26** (8), 080901.

ZHOU, Y., GROOM, M. & THORNBER, B. 2020*a* Dependence of enstrophy transport and mixed mass on dimensionality and initial conditions in the Richtmyer–Meshkov instability induced flows. *Trans. ASME J. Fluids Engng* **142** (12), 121104.

ZHOU, Y., *et al*. 2021 Rayleigh–Taylor and Richtmyer–Meshkov instabilities: a journey through scales. *Physica* D **423**, 132838.

https://doi.org/10.1017/jfm.2023.333 Published online by Cambridge University Press

ZHOU, Z., DING, J., ZHAI, Z., CHENG, W. & LUO, X. 2020*b* Mode coupling in converging Richtmyer–Meshkov instability of dual-mode interface. *Acta Mechanica Sin.* **36** (2), 356–366.

ZOU, L., AL-MAROUF, M., CHENG, W., SAMTANEY, R., DING, J. & LUO, X. 2019 Richtmyer–Meshkov instability of an unperturbed interface subjected to a diffracted convergent shock. *J. Fluid Mech.* **879**, 448–467.

https://doi.org/10.1017/jfm.2023.333 Published online by Cambridge University Press